AIP | Physics of Fluids

Reducing the data: Analysis of the role of vascular geometry on blood flow patterns in curved vessels

Jordi Alastruey, Jennifer H. Siggers, Véronique Peiffer, Denis J. Doorly, and Spencer J. Sherwin

Citation: Phys. Fluids **24**, 031902 (2012); doi: 10.1063/1.3694526
View online: http://dx.doi.org/10.1063/1.3694526
View Table of Contents: http://pof.aip.org/resource/1/PHFLE6/v24/i3
Published by the American Institute of Physics.

Reducing the data: Analysis of the role of vascular geometry on blood flow patterns in curved vessels

Jordi Alastruey,[1] Jennifer H. Siggers,[2] Véronique Peiffer,[2,3]
Denis J. Doorly,[3] and Spencer J. Sherwin[3]
[1]*Department of Biomedical Engineering, Division of Imaging Sciences and Biomedical Engineering, King's College London, King's Health Partners, St. Thomas' Hospital, London, SE1 7EH, United Kingdom*
[2]*Department of Bioengineering, Imperial College, London SW7 2AZ, United Kingdom*
[3]*Department of Aeronautics, Imperial College, London SW7 2AZ, United Kingdom*

(Received 6 October 2011; accepted 15 February 2012; published online 19 March 2012)

Three-dimensional simulations of blood flow usually produce such large quantities of data that they are unlikely to be of clinical use unless methods are available to simplify our understanding of the flow dynamics. We present a new method to investigate the mechanisms by which vascular curvature and torsion affect blood flow, and we apply it to the steady-state flow in single bends, helices, double bends, and a rabbit thoracic aorta based on image data. By calculating forces and accelerations in an orthogonal coordinate system following the centreline of each vessel, we obtain the inertial forces (centrifugal, Coriolis, and torsional) explicitly, which directly depend on vascular curvature and torsion. We then analyse the individual roles of the inertial, pressure gradient, and viscous forces on the patterns of primary and secondary velocities, vortical structures, and wall stresses in each cross section. We also consider cross-sectional averages of the in-plane components of these forces, which can be thought of as reducing the dynamics of secondary flows onto the vessel centreline. At Reynolds numbers between 50 and 500, secondary motions in the directions of the local normals and binormals behave as two underdamped oscillators. These oscillate around the fully developed state and are coupled by torsional forces that break the symmetry of the flow. Secondary flows are driven by the centrifugal and torsional forces, and these are counterbalanced by the in-plane pressure gradients generated by the wall reaction. The viscous force primarily opposes the pressure gradient, rather than the inertial forces. In the axial direction, and depending on the secondary motion, the curvature-dependent Coriolis force can either enhance or oppose the bulk of the axial flow, and this shapes the velocity profile. For bends with little or no torsion, the Coriolis force tends to restore flow axisymmetry. The maximum circumferential and axial wall shear stresses along the centreline correlate well with the averaged in-plane pressure gradient and the radial displacement of the peak axial velocity, respectively. We conclude with a discussion of the physiological implications of these results.
 [http://dx.doi.org/10.1063/1.3694526]

I. INTRODUCTION

In recent years, numerical models using anatomical reconstruction techniques have generated a plethora of simulations of blood flow in three-dimensional (3D) patient-specific geometries (e.g., Refs. 1–4). The motivation behind these studies is typically to determine spatial distributions of flow-related quantities that are associated with disease localisation and which are affected by vascular geometry. For example, early atheroma (atherosclerotic lesion) is observed to develop preferentially at arterial branches and bends and many studies have investigated its correlation with regions of low or oscillatory wall shear stress (WSS).[5,6] There is evidence that vascular prostheses (e.g., bypass grafts, stents, and arterio-venous shunts) and surgical reconstructions with a geometry that enhances

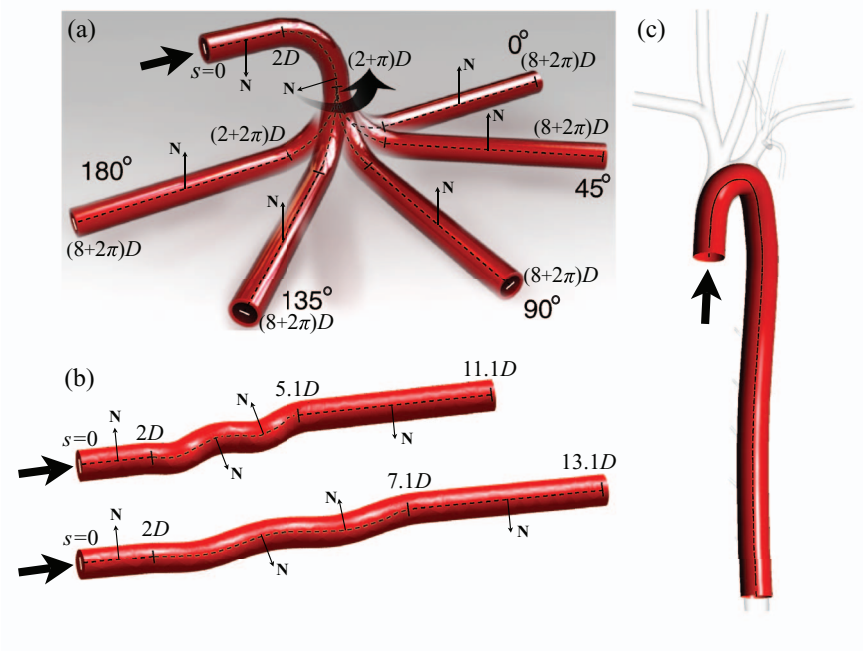

FIG. 1. The geometries studied: Single and double bends (a), helical bends (b), and rabbit thoracic aorta (c); each has uniform circular cross section of diameter D, the dashed line indicates the centreline of the pipe and the thick arrow indicates the inflow, where Poiseuille flow is prescribed. The local unit normal vector, **N**, and value of the arc length, s, are indicated at some locations (note that in straight regions **N** is not uniquely defined; here it has the same direction as in adjacent curved regions). (a) The azimuthal angles between the plane of curvature of each bend, whose curvature is $\kappa = \frac{1}{2D}$, are indicated in degrees (modified from Ref. 25). (b) The centrelines have a fixed helical radius of $D/8$ and a pitch length of $3D$ and $5D$. The inflow and outflow straight regions in (a) and (b) have lengths of $2D$ and $6D$, respectively. (c) A circular cross section of constant diameter (equal to the inlet diameter of the original aorta) was translated along the aortic centreline extracted from the original geometry in transparent grey (modified from Ref. 26).

in-plane mixing and produces more uniform WSS distributions are less prone to develop thrombosis and intimal hyperplasia (enlargement of the intimal layer of the vessel wall).[7]

It is therefore clinically relevant to understand the mechanisms underlying the relationship between vascular geometry and haemodynamics. Experimental, theoretical, and numerical studies have been carried out to study laminar flow in idealised geometries, such as flow around bends of constant curvature (e.g., Refs. 8–19) or helical tubes of constant curvature and torsion (e.g., Refs. 15 and 20–23). In some cases, it is possible to reduce the set of parameters to a small number, a classic example of this being Dean flow.[10,11,15] However, the relevance of these solutions to flow in real blood vessels is not yet fully known, and hence the mechanisms responsible for some of the complex flow phenomena that are observed in the human vasculature are not well understood.[18,24–26] Usually, 3D simulations produce such large quantities of data that they are unlikely to be of clinical use unless methods are available to simplify our understanding of the flow dynamics. For example, methods have been developed to identify and quantify bulk-flow features using helicity-based descriptors[27–30] and coherent structures.[25,31–33]

The aim of this work is to investigate the effect of vascular curvature and torsion on flow patterns and wall stresses in the idealised vessels shown in Fig. 1. These are typical geometrical conditions found in the cardiovascular system. Moreover, we want to understand mechanisms underlying the coupling of flow features across segments of different curvature and torsion, and to see where asymptotic states are applicable under geometric conditions that are not treatable by direct mathematical analysis.

To achieve these goals, we express the Navier–Stokes equations in a coordinate system centred on the centreline of the vessel in question, which explicitly provides the inertial forces. These are the centrifugal and Coriolis forces, which depend on the curvature of the centreline, and the torsional

force, which depends on the torsion of the centreline. Using this approach, we can analyse the individual roles of the inertial, pressure gradient, and viscous forces on the patterns of primary and secondary flows, vortical structures, and wall stresses in each cross section. Thus, we can separate inertial effects, which directly depend on vascular geometry, from the effect of the pressure gradient and viscous forces. We also work in terms of cross-sectional averages of the in-plane components of these forces. We study the evolution and interaction of these averages along the centreline to explore to what extent it is possible to reduce the dynamics of secondary flows onto the vessel centreline.

In this initial work we will only consider steady-state, Newtonian flows in uniform, fixed-wall geometries with circular cross sections and without branches. Analysis of these flows with our new method will give valuable insight into the role of vascular geometry, which should facilitate the interpretation of more complex unsteady flows in deformable walls.

We describe our numerical model in Sec. II and our post-processing technique in Sec. III. In Sec. IV, we study steady-flow patterns in the particular idealised bends and the rabbit thoracic aorta shown in Fig. 1, and we draw some conclusions in Sec. V. We list the abbreviations used in this paper in the supplementary material.[46]

II. NUMERICAL SOLUTIONS

The continuity and Navier–Stokes equations for steady, incompressible, Newtonian, and laminar flow were solved using a Cartesian coordinate system in the fixed geometries of Fig. 1 by a spectral/*hp* finite element method until convergence to steady flow was established.[25,26,34] We neglected gravity and prescribed Poiseuille flow at the inflow, a zero velocity gradient at the outflow, and no-slip velocity conditions at the vessel walls.

We define the Reynolds and Dean numbers as $Re = \overline{U}D/\nu$ and $De = 4Re\sqrt{D\kappa}$, respectively, where $\overline{U}$ is the average inflow velocity, D is the luminal diameter, ν is the kinematic viscosity of blood, and κ is the curvature of the centreline. Taking $\overline{U}$ and D equal to unity implicitly non-dimensionalises the problem, so that the modelled flow regimes depend on ν only. We consider $Re \in [50, 500]$ for the idealised geometries shown in Figs. 1(a) and 1(b). This range is chosen to be representative of physiological conditions in medium sized human arteries.[35] It corresponds to $De \in [141, 1414]$ for the bends and $De \in [87, 1428]$ for the helices. For the rabbit aorta (Fig. 1(c)) we use $Re = 300$.[26]

III. CENTRELINE ANALYSIS OF THE FLOW DYNAMICS

Figure 2 shows a sketch that summarises our centreline analysis and introduces some notation. In this section we show how to express the Navier–Stokes equations in local coordinates (Sec. III A), which allow us to obtain the inertial forces explicitly (Sec. III B). We define the cross-sectional averages used to reduce the dynamics of secondary flows onto the vessel centreline (Sec. III C) and show how to calculate flow vorticity and wall shear stress in local coordinates (Sec. III D).

A. Governing equations in local coordinates

We parameterise the centreline of a curved vessel by its arc length, s, and work in terms of the vector position $\mathbf{R}(s)$, unit tangent vector $\mathbf{T}(s)$, unit normal vector $\mathbf{N}(s)$ (pointing towards the local centre of curvature of the centreline C), and unit binormal vector $\mathbf{B}(s)$, which are related by

$$\mathbf{T} = \frac{\mathrm{d}\mathbf{R}}{\mathrm{d}s}, \quad \mathbf{N} = \frac{1}{\kappa}\frac{\mathrm{d}\mathbf{T}}{\mathrm{d}s}, \quad \mathbf{B} = \mathbf{T} \times \mathbf{N}, \tag{1}$$

where $\kappa(s) = |d^2\mathbf{R}/ds^2|$ is the curvature of the centreline. The Frenet–Serret formulae provide expressions for the rates of change of the unit vectors along the centreline,

$$\frac{d\mathbf{T}}{ds} = \kappa\mathbf{N}, \quad \frac{\mathrm{d}\mathbf{N}}{\mathrm{d}s} = \tau\mathbf{B} - \kappa\mathbf{T}, \quad \frac{\mathrm{d}\mathbf{B}}{\mathrm{d}s} = -\tau\mathbf{N}, \tag{2}$$

where $\tau(s)$ is the torsion of the centreline.

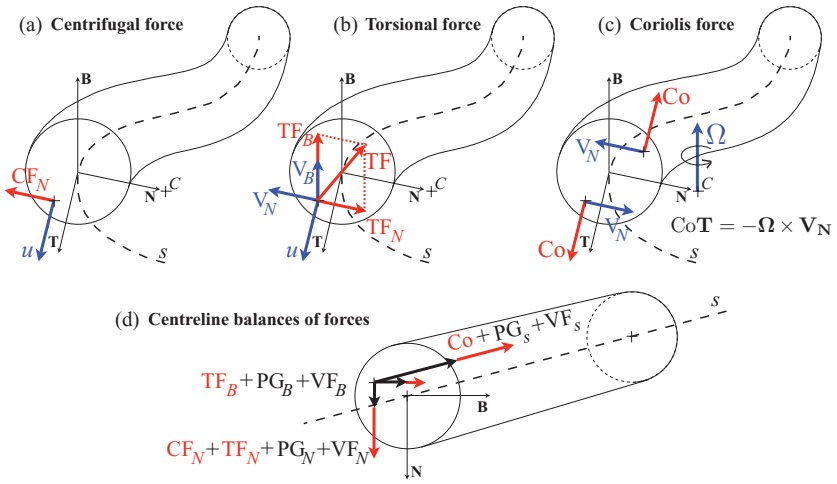

FIG. 2. Illustration of our centreline analysis. (a) The curvature-dependent centrifugal force, CF_N, always yields accelerations in the direction of the local normal, **N**, away from the centre of curvature, *C*, from axial (in the direction of the local tangent **T**) motions with velocity *u*. The local binormal is **B**. (b) The torsion-dependent force, TF, couples the normal and binormal components of secondary motions: it has normal, TF_N, and binormal, TF_B, components that depend on the binormal, V_B, and normal, V_N, velocities, respectively, generated by CF_N. (c) The curvature-dependent Coriolis force, Co, links normal motions to axial accelerations through the cross product $-\boldsymbol{\Omega} \times \mathbf{V_N}$, where $\boldsymbol{\Omega}$ is the angular velocity of the axial motions about *C*. (d) In local coordinates we can study the individual effect on the flow and wall stresses of the inertial (CF_N, TF_N, TF_B, and Co), pressure gradient (PG), and viscous (VF) forces in each cross section using the same orientation; i.e., cross sections can be thought of being aligned in a straight centreline, with the curvature and torsion of the vessel centreline (in dashed lines) replaced with the inertial forces.

We use Germano's orthogonal coordinate system (s, r, θ), which is defined uniquely for $r \leq 1/\kappa$, where *r* and θ are polar coordinates centred on the point $\mathbf{R}(s)$ in the plane normal to the centreline (Fig. 3). Any Cartesian position vector **x** can be uniquely expressed in these coordinates as[20]

$$\mathbf{x} = \mathbf{R} - r\sin(\theta+\phi)\mathbf{N} + r\cos(\theta+\phi)\mathbf{B}, \qquad \phi(s) = -\int_{s_0}^{s} \tau(s')ds', \tag{3}$$

where s_0 takes an arbitrary value. The unit vectors parallel to the local coordinate directions are defined as

$$\mathbf{a}_s = \mathbf{T}, \qquad \mathbf{a}_r = \cos(\theta+\phi)\mathbf{B} - \sin(\theta+\phi)\mathbf{N}, \qquad \mathbf{a}_\theta = -\sin(\theta+\phi)\mathbf{B} - \cos(\theta+\phi)\mathbf{N}.$$

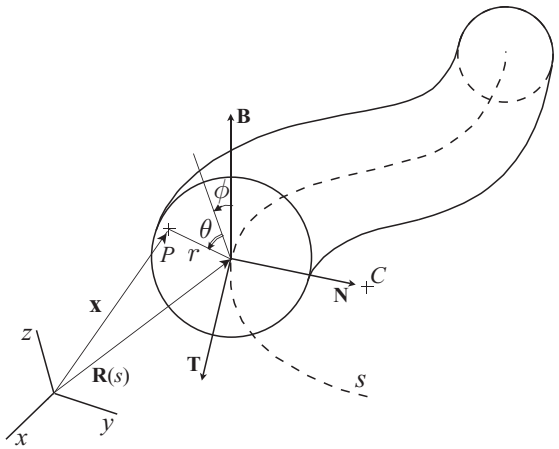

FIG. 3. Germano's coordinate system (s, r, θ) along the centreline of a generic vessel.[20]

Combining Eqs. (1)–(3) we obtain the orthogonal metric

$$\mathrm{d}\mathbf{x}\cdot\mathrm{d}\mathbf{x} = (h\,ds)^2 + (dr)^2 + (r\,d\theta)^2\,, \tag{4}$$

where $h = 1 + \kappa r \sin(\theta+\phi)$ (note that $h\kappa^{-1}$ is the distance from the local centre of curvature of the vessel centreline to the projection of the point into the plane spanned by **T** and **N**), and

$$\frac{\partial h}{\partial s} = \frac{\mathrm{d}\kappa}{\mathrm{d}s} r\sin(\theta+\phi) - \tau\kappa r\cos(\theta+\phi), \qquad \frac{\partial h}{\partial r} = \kappa\sin(\theta+\phi), \qquad \frac{\partial h}{\partial \theta} = \kappa r\cos(\theta+\phi).$$

We define the velocity components, u, v, and w, in the three coordinate directions $\mathbf{a}_s$, $\mathbf{a}_r$, $\mathbf{a}_\theta$, respectively, the fluid kinematic pressure, p, and the blood density, ρ. Following the technique described in Ref. 36, we can express the continuity and Navier–Stokes equations in local coordinates (s, r, θ) with the metric (4) as

$$\frac{1}{h}\frac{\partial u}{\partial s} + \frac{\partial v}{\partial r} + \frac{1}{r}\frac{\partial w}{\partial \theta} + \frac{v}{r} + \frac{\kappa}{h}\left[v\sin(\theta+\phi) + w\cos(\theta+\phi)\right] = 0, \tag{5}$$

$$\mathrm{CA}_s = \mathrm{Co} + \mathrm{PG}_s + \mathrm{VF}_s, \tag{6}$$

$$\mathrm{CA}_r = \mathrm{CF}_r + \mathrm{PG}_r + \mathrm{VF}_r, \tag{7}$$

$$\mathrm{CA}_\theta = \mathrm{CF}_\theta + \mathrm{PG}_\theta + \mathrm{VF}_\theta, \tag{8}$$

where

$$\mathrm{CA}_s = \mathcal{D}u, \qquad \mathrm{Co} = -\frac{\kappa u}{h}\left[v\sin(\theta+\phi) + w\cos(\theta+\phi)\right], \qquad \mathrm{PG}_s = -\frac{1}{\rho h}\frac{\partial p}{\partial s},$$

$$\mathrm{VF}_s = \nu\left\{\frac{\partial^2 u}{\partial r^2} + \frac{1}{r^2}\frac{\partial^2 u}{\partial \theta^2} + \frac{1}{r}\frac{\partial u}{\partial r} + \frac{\kappa}{h}\left[\frac{\partial u}{\partial r} - \frac{u}{h}\frac{\partial h}{\partial r}\right]\sin(\theta+\phi)\right.$$
$$\left. + \frac{\kappa}{hr}\left[\frac{\partial u}{\partial \theta} - \frac{u}{h}\frac{\partial h}{\partial \theta}\right]\cos(\theta+\phi) + \frac{1}{h^2}\left[\frac{\partial h}{\partial r}\frac{\partial v}{\partial s} + \frac{1}{r}\frac{\partial h}{\partial \theta}\frac{\partial w}{\partial s}\right] - \frac{1}{h}\left[\frac{\partial^2 v}{\partial s\partial r} + \frac{1}{r}\frac{\partial v}{\partial s} + \frac{1}{r}\frac{\partial^2 w}{\partial s\partial \theta}\right]\right\},$$

$$\mathrm{CA}_r = \mathcal{D}v - \frac{w^2}{r}, \qquad \mathrm{CF}_r = \frac{\kappa}{h}u^2\sin(\theta+\phi), \qquad \mathrm{PG}_r = -\frac{1}{\rho}\frac{\partial p}{\partial r},$$

$$\mathrm{VF}_r = \nu\left\{\frac{1}{h^2}\left[\frac{\kappa u}{h}\frac{\partial h}{\partial s} - \frac{\mathrm{d}\kappa}{\mathrm{d}s}u - \kappa\frac{\partial u}{\partial s}\right]\sin(\theta+\phi) + \frac{\tau\kappa}{h^2}u\cos(\theta+\phi)\right.$$
$$- \frac{\kappa}{h}\left[\frac{\partial w}{\partial r} + \frac{w}{r} - \frac{1}{r}\frac{\partial v}{\partial \theta}\right]\cos(\theta+\phi) - \frac{1}{h}\left[\frac{\partial^2 u}{\partial r\partial s} - \frac{1}{h}\frac{\partial^2 v}{\partial s^2} + \frac{1}{h^2}\frac{\partial h}{\partial s}\frac{\partial v}{\partial s}\right]$$
$$\left. - \frac{1}{r}\left[\frac{\partial^2 w}{\partial r\partial \theta} + \frac{1}{r}\frac{\partial w}{\partial \theta} - \frac{1}{r}\frac{\partial^2 v}{\partial \theta^2}\right]\right\},$$

$$\mathrm{CA}_\theta = \mathcal{D}w + \frac{vw}{r}, \qquad \mathrm{CF}_\theta = \frac{\kappa}{h}u^2\cos(\theta+\phi), \qquad \mathrm{PG}_\theta = -\frac{1}{\rho r}\frac{\partial p}{\partial \theta},$$

$$\mathrm{VF}_\theta = \nu\left\{\frac{1}{h^2}\left[\frac{\kappa u}{h}\frac{\partial h}{\partial s} - \frac{\mathrm{d}\kappa}{\mathrm{d}s}u - \kappa\frac{\partial u}{\partial s}\right]\cos(\theta+\phi) - \frac{\tau\kappa}{h^2}u\sin(\theta+\phi)\right.$$
$$+ \frac{\kappa}{h}\left[\frac{\partial w}{\partial r} + \frac{w}{r} - \frac{1}{r}\frac{\partial v}{\partial \theta}\right]\sin(\theta+\phi) - \frac{1}{h}\left[\frac{1}{r}\frac{\partial^2 u}{\partial \theta\partial s} - \frac{1}{h}\frac{\partial^2 w}{\partial s^2} + \frac{1}{h^2}\frac{\partial h}{\partial s}\frac{\partial w}{\partial s}\right]$$
$$\left. - \frac{1}{r}\left[\frac{\partial^2 v}{\partial r\partial \theta} - \frac{1}{r}\frac{\partial v}{\partial \theta} - \frac{\partial w}{\partial r} + \frac{w}{r}\right] + \frac{\partial^2 w}{\partial r^2}\right\},$$

and

$$\mathcal{D} = \frac{u}{h}\frac{\partial}{\partial s} + v\frac{\partial}{\partial r} + \frac{w}{r}\frac{\partial}{\partial \theta}.$$

The terms CA, CF, PG, and VF, respectively denote the convective acceleration and the centrifugal, pressure gradient, and viscous forces per unit of mass. Their axial, radial, and circumferential components are, respectively, indicated by the subscripts s, r, and θ. In the Appendix we provide formulae to convert the velocity, its first and second derivatives, and the pressure gradient from Cartesian (x, y, z) to local (s, r, θ) coordinates.

Equations (5)–(8) reduce to the continuity and Navier–Stokes equations in toroidal coordinates if $\tau = 0$ and κ is constant, and in cylindrical coordinates in the special case $\tau = 0$ and $\kappa = 0$.

In Sec. III B we find expressions for the components of the forces, accelerations, and velocities in the natural directions **T**, **N**, and **B**, which provide the inertial forces explicitly.

B. Inertial forces

1. Coriolis force

The quantities in Eq. (6) are already resolved in the direction of **T**, since $\mathbf{a}_s = \mathbf{T}$. To interpret Co, we transform the velocity field $\mathbf{V} = (u, v, w)$ at the point $\mathbf{R}(s)$ to a coordinate system rotating with angular velocity $\mathbf{\Omega} = \Omega(s, r, \theta)\mathbf{B}$ about C (note that the local angular velocity about C is $u\kappa h^{-1}$, but for now we allow general Ω). The velocity components of a fluid element at a particular (s, r, θ) with respect to this coordinate system are $(\hat{u}, v, w)$, with $u = \hat{u} + h\kappa^{-1}\Omega$. Substitution of this expression for u into CA_s and Co in Eq. (6) yields

$$\mathrm{CA}_s(u) = \mathrm{CA}_s(\hat{u}) - \Omega V_N + \frac{\Omega}{\kappa}\left[\frac{\partial \hat{u}}{\partial s} + u\frac{\partial}{\partial s}(\ln h - \ln \kappa)\right] + \frac{h}{\kappa}\mathcal{D}\Omega, \tag{9}$$

$$\mathrm{Co}(u) = \mathrm{Co}(\hat{u}) + \Omega V_N, \tag{10}$$

where $V_N = -v\sin(\theta + \phi) - w\cos(\theta + \phi)$ is the component of the secondary motion in the direction of **N** with respect to both the rotating and local frames. The term ΩV_N in Eqs. (9) and (10) satisfies $\Omega V_N \mathbf{T} = -\mathbf{\Omega} \times \mathbf{V_N}$, where $\mathbf{V_N} = V_N \mathbf{N}$ (Fig. 2(c)). With the choice $\Omega = u\kappa h^{-1}$, then $\hat{u} = 0$ (i.e., the rotating frame is moving with the local axial velocity u at a particular (s, r, θ)) and

$$\mathrm{CA}_s(u) = -\Omega V_N + \frac{u^2}{h}\frac{\partial}{\partial s}(\ln h - \ln \kappa) + \frac{h}{\kappa}\mathcal{D}\Omega, \tag{11}$$

$$\mathrm{Co}(u) = \Omega V_N. \tag{12}$$

Equation (12) shows that $\mathrm{Co}\mathbf{T} = -\mathbf{\Omega} \times \mathbf{V_N}$; i.e., Co is half of the usual Coriolis force (per unit of mass) arising from the curvature of the vessel, κ, normal velocity, V_N, and axial velocity, u. The other half arises from CA_s as shown in Eq. (11).

2. Centrifugal and torsional forces

We obtain the centrifugal and torsional forces by projecting the quantities appearing in Eqs. (7) and (8) in the **N** and **B** directions. We use the subscripts N and B to denote components of quantities in the directions **N** and **B**, respectively, and the relationships

$$\xi_N = -\xi_r \sin(\theta + \phi) - \xi_\theta \cos(\theta + \phi), \qquad \xi_B = \xi_r \cos(\theta + \phi) - \xi_\theta \sin(\theta + \phi),$$

where ξ is one of CA, CF, PG, or VF, to obtain

$$\mathrm{CA}_N = \frac{u}{h}\left(\frac{\partial V_N}{\partial s} - \tau V_B\right) + V_N\frac{\partial V_N}{\partial n} + V_B\frac{\partial V_N}{\partial b}, \tag{13}$$

$$\mathrm{CA}_B = \frac{u}{h}\left(\frac{\partial V_B}{\partial s} + \tau V_N\right) + V_B\frac{\partial V_B}{\partial b} + V_N\frac{\partial V_B}{\partial n}, \tag{14}$$

$$\mathrm{CF}_N = -\frac{\kappa u^2}{h}, \quad \mathrm{CF}_B = 0, \tag{15}$$

$$\mathrm{PG}_N = -\frac{1}{\rho}\frac{\partial p}{\partial n}, \quad \mathrm{PG}_B = -\frac{1}{\rho}\frac{\partial p}{\partial b}, \tag{16}$$

where CF_N is the centrifugal force (Fig. 2(a)). In these equations, $\partial/\partial s$, $\partial/\partial n$, $\partial/\partial b$ denote the components of the gradient vector in the directions **T**, **N**, **B**, respectively, $V_B = v\cos(\theta + \phi) - w\sin(\theta + \phi)$ is the component of the secondary motion in the direction of **B**, and $n = -r\sin(\theta + \phi)$ and $b = r\cos(\theta + \phi)$ are the components of the displacement from the centreline in the directions of **N** and **B**, respectively. We now define the local torsional force (0, TF_N, TF_B) (Fig. 2(b)) by

$$\mathrm{TF}_N = \frac{\tau u}{h}V_B, \quad \mathrm{TF}_B = -\frac{\tau u}{h}V_N, \tag{17}$$

resulting in modified convective accelerations CA'_N and CA'_B,

$$\mathrm{CA}'_N = \frac{u}{h}\frac{\partial V_N}{\partial s} + V_N\frac{\partial V_N}{\partial n} + V_B\frac{\partial V_N}{\partial b}, \tag{18}$$

$$\mathrm{CA}'_B = \frac{u}{h}\frac{\partial V_B}{\partial s} + V_B\frac{\partial V_B}{\partial b} + V_N\frac{\partial V_B}{\partial n}, \tag{19}$$

so that the balance of in-plane momentum takes the form

$$\mathrm{CA}'_N = \mathrm{CF}_N + \mathrm{TF}_N + \mathrm{PG}_N + \mathrm{VF}_N, \tag{20}$$

$$\mathrm{CA}'_B = \mathrm{TF}_B + \mathrm{PG}_B + \mathrm{VF}_B. \tag{21}$$

Note that the components of the convective acceleration with respect to a fixed Cartesian reference frame are $\mathrm{CA}_s - \mathrm{Co}$, $\mathrm{CA}'_N - \mathrm{CF}_N - \mathrm{TF}_N$, and $\mathrm{CA}'_B - \mathrm{TF}_B$ in the directions **T**, **N**, and **B**, respectively. In local coordinates, we can explicitly separate the inertial forces Co, CF_N, TF_N, and TF_B, which simplify the analysis of the effect of curvature κ and torsion τ on flow patterns (Fig. 2(d)).

C. Cross-sectional averages

Given a field $\xi(s, r, \theta)$ and a point $\mathbf{R}(s)$ on the centreline, we define the cross-sectional average of the field, $\overline{\xi}$, to be

$$\overline{\xi} = \frac{1}{S}\int_S \xi \,\mathrm{d}A, \tag{22}$$

where $S(s)$ is the flat cross section that is normal to the centreline at $\mathbf{R}(s)$ and $\mathrm{d}A = r\mathrm{d}r\mathrm{d}\theta$. Hereinafter, a line over a field name denotes its cross-sectional average.

D. Vorticity and wall shear stress

The components of the vorticity vector $\boldsymbol{\omega} = \nabla \times (u, v, w)$ in local coordinates are[36]

$$\omega_s = \frac{1}{r}\frac{\partial(rw)}{\partial r} - \frac{1}{r}\frac{\partial v}{\partial \theta}, \qquad \omega_r = \frac{1}{rh}\left[\frac{\partial(hu)}{\partial \theta} - r\frac{\partial w}{\partial s}\right], \qquad \omega_\theta = \frac{1}{h}\left[\frac{\partial v}{\partial s} - \frac{\partial(hu)}{\partial r}\right].$$

In local coordinates, the axial WS_s and circumferential WS_θ WSS take the form

$$WS_s = -\nu\rho \left.\frac{\partial u}{\partial r}\right|_{r=D/2}, \qquad WS_\theta = -\nu\rho \left.\frac{\partial w}{\partial r}\right|_{r=D/2}, \tag{23}$$

respectively, so that the tangential traction exerted by the wall on the flow is $\boldsymbol{WS} = -(WS_s, 0, WS_\theta)$. At the wall surface ($r = D/2$), $\boldsymbol{WS} = \nu\rho\boldsymbol{\omega} \times \boldsymbol{n}$ is satisfied, where $\boldsymbol{n}$ is the wall normal. This expression leads to

$$WS_s = \nu\rho\omega_\theta|_{r=D/2}, \qquad WS_\theta = -\nu\rho\omega_s|_{r=D/2}. \tag{24}$$

IV. RESULTS AND DISCUSSION

We first focus on the in-plane flow patterns in the single bend and small-amplitude helical tubes shown in Figs. 1(a) and 1(b). Thus, we first investigate the effect of curvature κ in isolation using the single bend, and the combined effect of both κ and torsion τ using the helices. We will describe the in-plane forces responsible for the flow patterns in local coordinates (Sec. IV A) and study how forces interact along the centreline by analysing their cross-sectional averages in the normal and binormal directions (Sec. IV B). We then study the effect of κ and τ on the axial flow (Sec. IV C), including the role of the full Coriolis force 2Co. After investigating these simplified geometries, we will apply the knowledge gained to study the effect of κ and τ on the flow in the double bends (Sec. IV D) and rabbit thoracic aorta (Sec. IV E), which was reconstructed from images neglecting tapering and side branches (Fig. 1(c)). In Sec. IV F, we study the effect of κ and τ on wall stresses.

The bends in Fig. 1(a) loosely model a bypass graft in a peripheral vessel with the proximal branch of the host vessel occluded. The small-amplitude helical tubes in Fig. 1(b) were recently studied for potential application as vascular prostheses, since they promote in-plane mixing.[7,23]

All the cross-sectional contours are shown normal to the local tangent vector **T**, with the directions of the local normal **N** and binormal **B** vectors as indicated in the figures. The computational errors in the net balance of mass and momentum are similar in Cartesian and local coordinates, and are too small to be observed in the scales of the figures.

A. In-plane flow patterns in local coordinates

1. *Single bend: The role of the centrifugal force* CF_N

Figure 4 shows the centrifugal force (CF_N), the in-plane pressure gradient (PG), and viscous (VF) forces that develop to conserve momentum, and the resulting secondary flows, and accelerations at three locations in the single bend of Fig. 1(a) for $Re = 125$.

A pair of counter-rotating (Dean) vortices (Fig. 4(b)) is formed in the curve due to the interaction between the driving CF_N and the opposing in-plane PG in an essentially inviscid manner, as follows. At the start of the bend ($s = 2D$), the in-plane PG (Fig. 4(i)) is centripetal (in the direction of **N** and toward the centre of curvature) and smaller than CF_N (Fig. 4(g)) in the core flow, and circumferential and greater than CF_N near the wall. The resulting convective acceleration $\mathrm{CA}' = \mathrm{CA}$ (Fig. 4(d)) is centrifugal (in the direction of **N** and away from the centre of curvature) in the core flow and has a spiral pattern near $\theta = 0^\circ$ and $\theta = 180^\circ$ (hereinafter referred to as the "laterals").

As we move downstream (in the direction of **T**), the reaction of the wall to the persistent CF_N gradually increases the difference between the extremes of wall pressure (Fig. 4(w)). From $s = 2.1D$, the in-plane PG becomes larger than CF_N in the outer core. As a result, both regions of spiral CA at $s = 2D$ (Fig. 4(d)) are gradually transformed into two regions of radial CA (Fig. 4(e)) that persist up to $s = 8D$, generating the circular secondary motions that form the Dean vortices (Fig. 4(b)). In the core, fluid elements are swept by CF_N (Fig. 4(h)) to the outer wall, from where they flow toward the inner wall through the laterals, driven by PG (Fig. 4(j)) and opposed by VF (Fig. 4(m)) and the centrifugal wall traction $-WS_\theta$ (Fig. 4(x)). The directions of the in-plane VF (Figs. 4(m) and 4(n)) oppose the streamlines of secondary flows (Figs. 4(b) and 4(c)) and the axial vorticity, ω_s, generated

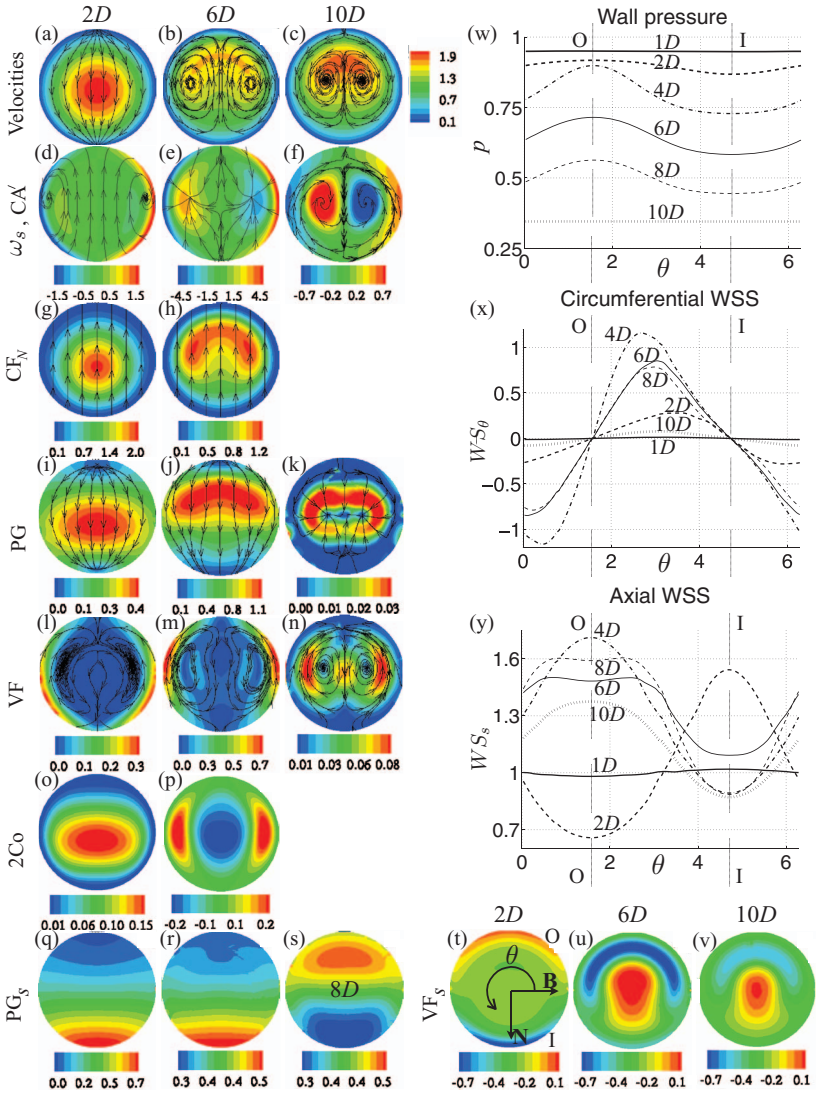

FIG. 4. (a)–(v) Contours of the magnitude of the following local quantities at $s = 2D$, $6D$, and $10D$ in the single bend (180° in Fig. 1(a)) for $Re = 125$: axial velocity with secondary-flow streamlines (a)–(c), axial vorticity, ω_s, with overlaid directions of the in-plane convective acceleration, $CA' = CA$, (d)–(f), centrifugal CF_N (g) and (h), in-plane pressure gradient PG (i)–(k) and in-plane viscous VF (l)–(n) forces per unit of mass with their directions overlaid, and axial full Coriolis 2Co (o) and (p), pressure gradient PG_s (q)–(s) and viscous VF_s (t)–(v) forces per unit of mass. Panel (s) shows PG_s at $s = 8D$ ($PG_s = 0.3$ at $s = 10D$). The local **N**, **B**, and θ are oriented as shown in (t), and CF_N and 2Co are zero at $s = 10D$. (w)–(y) Wall pressure p (w) and circumferential WS_θ (x) and axial WS_s (y) shear stresses with θ at the sites indicated by the labels. Pressures and shear stresses are non-dimensionalised by the uniform p and WS_s, respectively, at $s = 0$ (where we have Poiseuille flow). The dashed vertical lines indicate the outside (O, $\theta = 90°$) and inside (I, $\theta = 270°$) of the bend.

by the wall traction $-WS_\theta$ (see Eq. (24)), forms vortex sheets that oppose the ω_s of the Dean vortices (Figs. 4(d)–4(f)).

As the Reynolds number Re increases, the in-plane PG increases to counterbalance CF_N, generating more wall vorticity ω_s that is convected by the flow to the core with less viscous dissipation, following Helmholtz's laws of vorticity (Ref. 37, pp. 186–188). Additional pairs of counter-rotating vortices develop, as Figs. 5(a)–5(e) show at $s = 6D$ when Re increases from 50 to 500. The directions of in-plane CA tend to point at the centres of vortices (Figs. 5(g)–5(k)), supporting theoretical results[38] and confirming that CF_N should be regarded as a force (and not as part of the in-plane CA) in local coordinates. This is also the case for the torsional force TF (Sec. IV A 2).

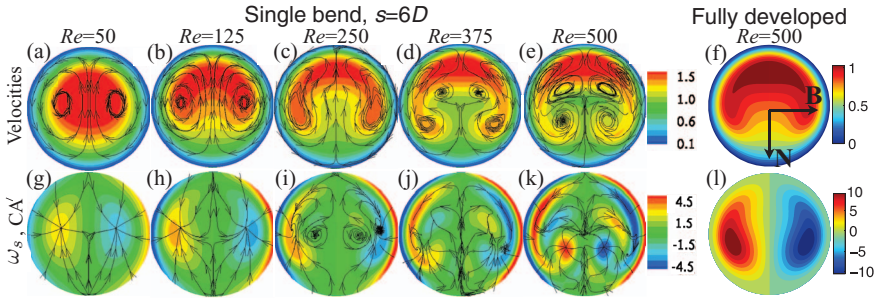

FIG. 5. Axial velocity (top) and vorticity (bottom) contours at $s = 6D$ in the single bend (180° in Fig. 1(a)) for $Re = 50$ (a) and (g), 125 (b) and (h), 250 (c) and (i), 375 (d) and (j), and 500 (e) and (k). The secondary-flow streamlines and directions of in-plane convective acceleration, $CA' = CA$, are overlaid within the velocity and vorticity contours, respectively. Axial velocity (f) and vorticity (l) for the fully developed flow at $Re = 500$, calculated using the asymptotic model in Ref. 17. The local **N** and **B** are oriented as shown in (f).

2. *Helical pipes: The role of the torsional force TF*

If torsion τ is nonzero, the torsional force TF has two in-plane components, TF_N and TF_B, which depend on the secondary motions V_B and V_N, respectively, Eq. (17), which are generated by the centrifugal force CF_N (the pattern of CF_N at $s = 2D$ in the helical bends is similar to the pattern shown in Fig. 4(g) for the single bend). Figure 6 shows TF and other in-plane quantities at three locations in the helix with a pitch length of $3D$ (Fig. 1(b)) and $Re = 125$. The patterns of secondary velocities, axial vorticity ω_s, and in-plane convective acceleration (CA') and torsional (TF), pressure gradient (PG), and viscous (VF) forces per unit of mass shown at $s = 4D$ are similar to those obtained in most of the helix, except for its inlet and outlet regions.

At the start of the helix, secondary motions (Fig. 6(a)) are generated by the in-plane PG (the patterns of PG in Fig. 6(i) are similar to the secondary motions in Fig. 6(a)), which gradually builds its opposition to CF_N and TF before the helix starts. To counterbalance TF_B (Fig. 6(g)), the PG is skewed toward the (**N**, **B**)–quadrant (i.e., the quadrant bounded by **N** and **B** in Fig. 6(t)). Thus, the torsional force breaks the flow symmetry. The resulting acceleration CA' starts rotating the flow in two locations near the lateral walls (Fig. 6(d)), a few degrees anticlockwise from the spiral regions at the laterals of the single bend (Fig. 4(d)).

Downstream, CF_N turns V_N into centrifugal in the core flow, so that TF_B becomes positive in the core, as dictated by Eq. (17). As a result, the secondary-flow streamlines in the core are directed toward the (-**N**,**B**)–quadrant (Figs. 6(b) and 6(c)), rotating the positions of the centres of the two vortices clockwise (Figs. 6(e) and 6(f)). Moreover, TF (Fig. 6(h)) expands the outer vortex (Figs. 6(b) and 6(e)) by accelerating fluid particles away from its centre of rotation and pushing the inner vortex toward the (**N**,**B**)–quadrant. These effects are more pronounced with increasing torsion τ and Dean number De. As in the single bend, the directions of in-plane VF (Figs. 6(m) and 6(n)) oppose the streamlines of secondary flows (Figs. 6(b) and 6(c)).

B. Cross-sectional averages of in-plane forces and accelerations

In all the geometries studied, the cross-sectionally averaged convective acceleration in the direction of **N**, $\overline{CA'_N}$, is almost proportional to the change with s of the cross-sectionally averaged normal velocity, $\partial\overline{V_N}/\partial s$, and $\overline{CA'_B}$ is almost proportional to $\partial\overline{V_B}/\partial s$ (Figs. 7, 14(a), and 14(b)), since (i) the last two terms on the right of both Eqs. (18) and (19) are negligible compared to the first, when cross-sectionally averaged, (ii) $\overline{u/h\,\partial V_N/\partial s}$ is approximately proportional to $\partial\overline{V_N}/\partial s$, and (iii) $\overline{u/h\,\partial V_B/\partial s}$ is approximately proportional to $\partial\overline{V_B}/\partial s$. Therefore, the patterns of the averaged velocities $\overline{V_N}$ and $\overline{V_B}$ with s are mainly governed by the averaged forces in the direction of **N** ($\overline{CF_N}$, $\overline{TF_N}$, $\overline{PG_N}$, and $\overline{VF_N}$) and **B** ($\overline{TF_B}$, $\overline{PG_B}$, and $\overline{VF_B}$), respectively. Next we study how these sectionally averaged forces interact along the centreline of the single-bend and helical geometries.

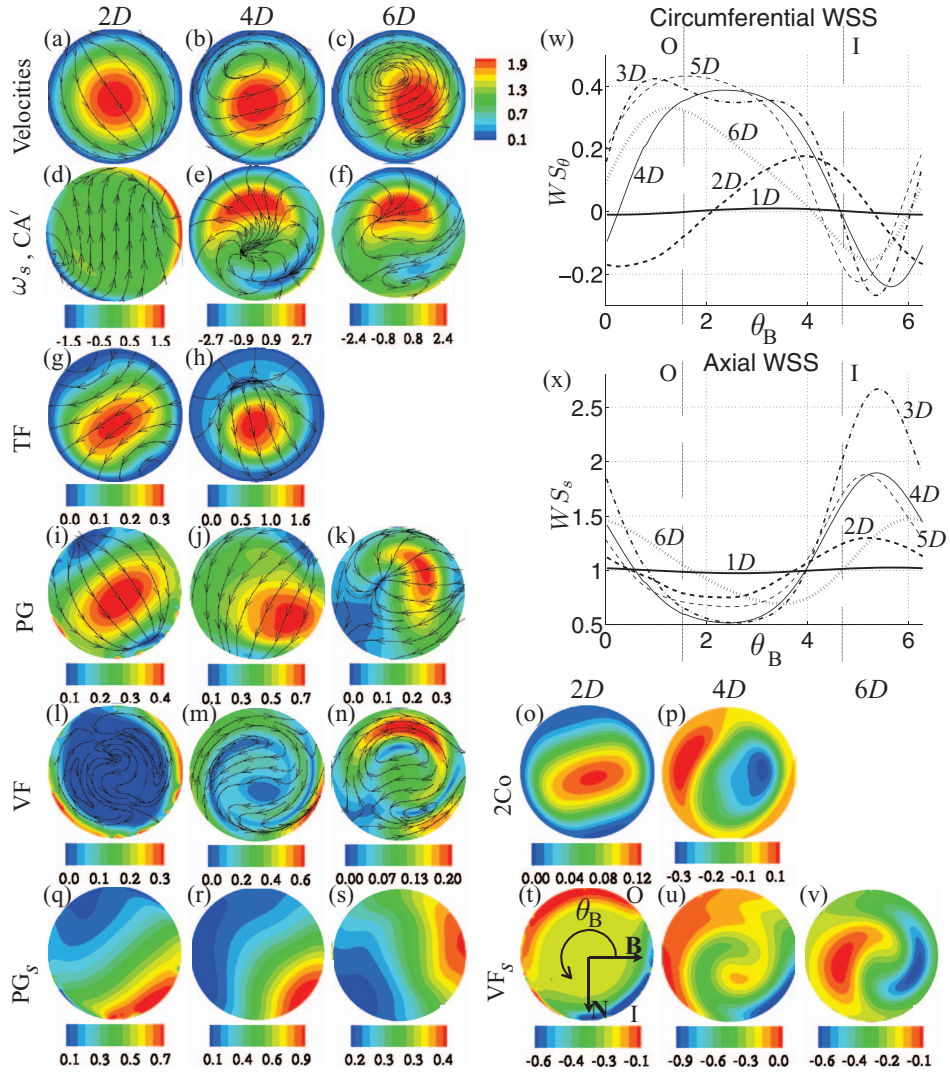

FIG. 6. (a)–(v) Contours of the magnitude of the following local quantities at $s = 2D$, $4D$, and $6D$ in the helical bend with a pitch length of $3D$ (Fig. 1(b)) and $Re = 125$: axial velocity with secondary-flow streamlines (a)–(c), axial vorticity, ω_s, with overlaid directions of the in-plane convective acceleration, CA′, (d)–(f), torsional TF (g) and (h), in-plane pressure gradient PG (i)–(k) and in-plane viscous VF (l)–(n) forces per unit of mass with their directions overlaid, and axial full Coriolis 2Co (o) and (p), pressure gradient PG_s (q)–(s) and viscous VF_s (t)–(v) forces per unit of mass. TF and 2Co are zero at $s = 6D$. (w) and (x) Circumferential WS_θ (w) and axial WS_s (x) wall shear stresses with the circumferential angle θ_B, with origin in the direction of **B**, at the sites indicated by the labels. They are non-dimensionalised by the uniform (Poiseuille flow) WS_s at $s = 0$. The local **N**, **B**, and θ_B are oriented as shown in (t). The dashed vertical lines indicate the outside (O, $\theta_B = 90°$) and inside (I, $\theta_B = 270°$) of the bend.

1. Single bend

If torsional forces are absent, the symmetry of the Poiseuille inflow along the radius of curvature is not broken. Thus, the sectionally averaged quantities $\overline{V_B}$, $\overline{CA'_B}$, $\overline{PG_B}$, and $\overline{VF_B}$ are zero and $\overline{CA'_N} = \overline{CA_N}$ (see Eqs. (13) and (18)). Figure 8 shows $-\overline{CF_N}$, $\overline{PG_N}$, and $\overline{VF_N}$ for different Re in the single bend. A centripetal averaged normal pressure gradient, $\overline{PG_N}$, gradually develops $1D$ before entering the bend to anticipate the opposition to the discontinuous appearance of the averaged centrifugal force, $\overline{CF_N}$, at $s = 2D$. Before the bend ends, $\overline{PG_N}$ starts reducing to anticipate the discontinuous disappearance of $\overline{CF_N}$. Within the bend, $\overline{PG_N}$ opposes $\overline{CF_N}$ producing an oscillatory averaged normal convective acceleration, $\overline{CA_N}$, with an amplitude that increases with increasing Re

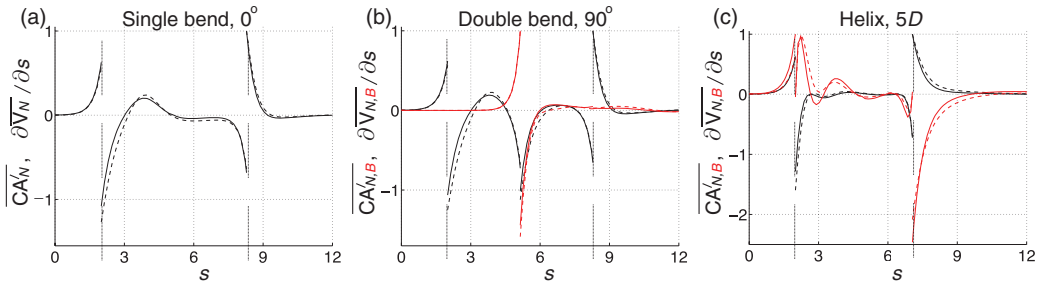

FIG. 7. Cross-sectional averages $\overline{CA'_N}$, $\overline{CA'_B}$ (dashed lines), $\frac{\partial \overline{V_N}}{\partial s}$, and $\frac{\partial \overline{V_B}}{\partial s}$ (solid lines) along the centreline of the (a) single bend, (b) double bend with a 90° azimuthal angle, and (c) helical bend with a pitch length of 5*D* (Figs. 1(a) and 1(b)) for *Re* = 125. They are non-dimensionalised by their corresponding maximum values and shown in black in the **N**–direction and in colour in the **B**–direction. The dashed vertical lines indicate the start and end of the curved regions.

and tends to zero as the flow develops with increasing *s*. For the fully developed state $\overline{V_N}$ and $\overline{CA_N}$ are zero and $\overline{PG_N} + \overline{CF_N} + \overline{VF_N} = 0$ (Table I).

Moreover, the averaged normal viscous force, $\overline{VF_N}$, opposes $\overline{PG_N}$ rather than $\overline{CF_N}$, since the in-plane VF_N (Figs. 4(l) and 4(m)) is larger near the wall to oppose centripetal velocities driven by PG_N (Figs. 4(i) and 4(j)) than in the core to oppose centrifugal velocities driven by CF_N (Figs. 4(g) and 4(h)). Indeed, $\overline{VF_N}$ is approximately proportional to $-\overline{PG_N}$ (Fig. 8).

At *Re* = 50 the flow becomes fully developed within less than 3*D* into the bend, as shown by the plateaus in the averages in Fig. 8(a). This entry length is much smaller than the 13.0*D* predicted using Yao and Berger's formula[39] for a uniform axial velocity at the start of a uniformly bent vessel. At *Re* = 125 the flow is close to full development after 4*D* in the bend, as indicated by $\overline{V_N}$ and $\overline{CA_N}$ becoming close to zero (Fig. 8(b)). Indeed, velocities, forces, and accelerations at $s = 6.75D$ are in good qualitative and quantitative agreement with their fully developed counterparts (Fig. 9). Significant discrepancies exist, however, for larger *Re*; *e.g.,* at *Re* = 500 there are three pairs of counter-rotating vortices at $s = 6D$ (Figs. 5(e) and 5(k)), but only one pair for the fully developed flow (Fig. 5(l)). Although the corresponding axial velocity profiles are similar (Figs. 5(e) and 5(f)), the oscillations of $\overline{CA_N}$ in Fig. 8(c) indicate the flow in the single bend is far from full development.

2. Helical pipes

Despite torsion τ being larger than curvature κ in our helices ($\kappa = 0.51/D$ and $\tau = 1.96/D$ for the pitch length of 3*D*; $\kappa = 0.19/D$ and $\tau = 1.23/D$ for the pitch length of 5*D*), the centripetal averaged normal torsional force, $\overline{TF_N}$, is smaller than the averaged centripetal force, $-\overline{CF_N}$ (Figs. 10(a) and 10(b)), since $\overline{TF_N}$ depends explicitly on the secondary velocities generated by CF_N, which are one order of magnitude smaller than axial velocities. Consequently, the averaged normal pressure

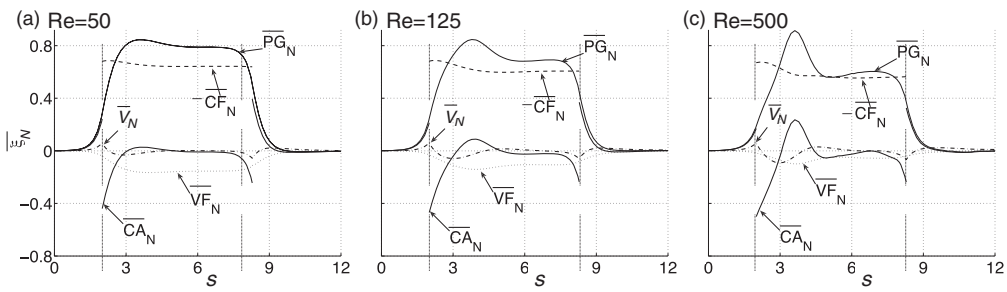

FIG. 8. Cross-sectionally averaged normal acceleration $\overline{CA_N} = \overline{CA'_N}$, forces per unit of mass $-\overline{CF_N}$, $\overline{PG_N}$, and $\overline{VF_N}$, and velocity $\overline{V_N}$ along the centreline of the single bend (180° in Fig. 1(a)) for (a) *Re* = 50, (b) 125, and (c) 500. Note that $-CF_N$ is centripetal. The dashed vertical lines indicate the start and end of the curved region.

TABLE I. Cross-sectionally averaged centrifugal, $\overline{\mathrm{CF}_N}$, pressure gradient, $\overline{\mathrm{PG}_N}$, and viscous, $\overline{\mathrm{VF}_N}$, forces per unit of mass for the fully developed flow at several *Re*. They were calculated using the model in Ref. 17.

Re	50	125	250	375	500
$\overline{\mathrm{CF}_N}$	− 0.64	− 0.61	− 0.60	− 0.59	− 0.58
$\overline{\mathrm{PG}_N}$	0.79	0.72	0.68	0.65	0.64
$\overline{\mathrm{VF}_N}$	− 0.15	− 0.11	− 0.08	− 0.07	− 0.06

gradient, $\overline{\mathrm{PG}_N}$, is centripetal to oppose $\overline{\mathrm{CF}_N}$, and not centrifugal to oppose the centripetal $\overline{\mathrm{TF}_N}$. Moreover, $\overline{\mathrm{PG}_N}$ anticipates discontinuous appearances and disappearances of $\overline{\mathrm{CF}_N}$, rather than those of $\overline{\mathrm{TF}_N}$. This observation is in line with the asymptotic analysis in Ref. 20, which shows the effects of κ and τ on the flow in a helical pipe are of first and second order, respectively, for κ and τ of the same order and small compared to the vessel diameter D. As τ increases, $\overline{\mathrm{TF}_N}$ grows relative to $\overline{\mathrm{CF}_N}$, weakening $\overline{\mathrm{PG}_N}$ relative to $\overline{\mathrm{CF}_N}$ (Figs. 10(a) and 10(b); note that Fig. 10(b) is for a helix with lower τ than in Fig. 10(a)).

In the binormal direction, $\overline{\mathrm{PG}_B}$ is negative to oppose $\overline{\mathrm{TF}_B}$ (Figs. 10(d) and 10(e)), except for the region around the helix entrance. About $1D$ before the helix starts, a positive $\overline{\mathrm{PG}_B}$ gradually develops to counterbalance the negative $\overline{\mathrm{TF}_B}$ at the helix entrance. Before the helix ends, the drop in $\overline{\mathrm{PG}_N}$ (to anticipate the discontinuous disappearance of $\overline{\mathrm{CF}_N}$) allows $\overline{\mathrm{CF}_N}$ to decrease the averaged normal velocity, $\overline{V_N}$ (Figs. 10(a) and 10(b)), so that $\overline{\mathrm{TF}_B}$ increases according to Eq. (17). This increase is counterbalanced by $\overline{\mathrm{PG}_B}$, which prevents greater changes in the averaged binormal acceleration, $\overline{\mathrm{CA}'_B}$ (Figs. 10(d) and 10(e)).

After $3D$ in the helix with a pitch length of $5D$ and at $Re = 125$, the plateaus in the cross-sectionally averages in the directions of **N** and **B**, and the tendency of the averaged accelerations $\overline{\mathrm{CA}'_N}$ and $\overline{\mathrm{CA}'_B}$ to zero (but not the averaged velocities $\overline{V_N}$ and $\overline{V_B}$ due to the asymmetry introduced by the torsional forces) (Figs. 10(b) and 10(e)) indicate that the flow is close to become fully developed.

3. Analogy with the underdamped oscillator

The previous results suggest that $\overline{\mathrm{CA}'_N}$ and $\overline{\mathrm{CA}'_B}$ play the role of the accelerations and $\overline{V_N}$ and $\overline{V_B}$ of the velocities of two underdamped oscillators, one for the normal and one for the binormal direction, around the fully developed state. In the normal direction, the centrifugal $\overline{\mathrm{CF}_N}$ and centripetal $\overline{\mathrm{TF}_N}$ are the driving forces, $\overline{\mathrm{PG}_N}$ is the restoring force, and $\overline{\mathrm{VF}_N}$ is the frictional force opposing $\overline{\mathrm{PG}_N}$ (Figs. 8, 10(a), and 10(b)). In the binormal direction, $\overline{\mathrm{TF}_B}$ is the driving force, $\overline{\mathrm{PG}_B}$ is the restoring force, and $\overline{\mathrm{VF}_B}$ is the frictional force opposing $\overline{\mathrm{PG}_B}$ (Figs. 10(d) and 10(e)). The two

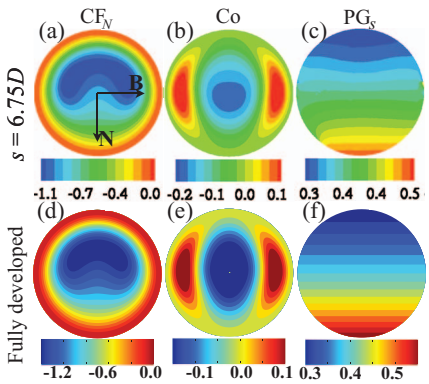

FIG. 9. Contours of the centrifugal, CF_N, Coriolis, Co, and axial pressure gradient, PG_s, forces per unit of mass for $Re = 125$, for the (top) single bend (180° in Fig. 1(a)) at $s = 6.75D$ and (bottom) fully developed flow calculated using the model in Ref. 17. The local **N** and **B** are oriented as shown in (a).

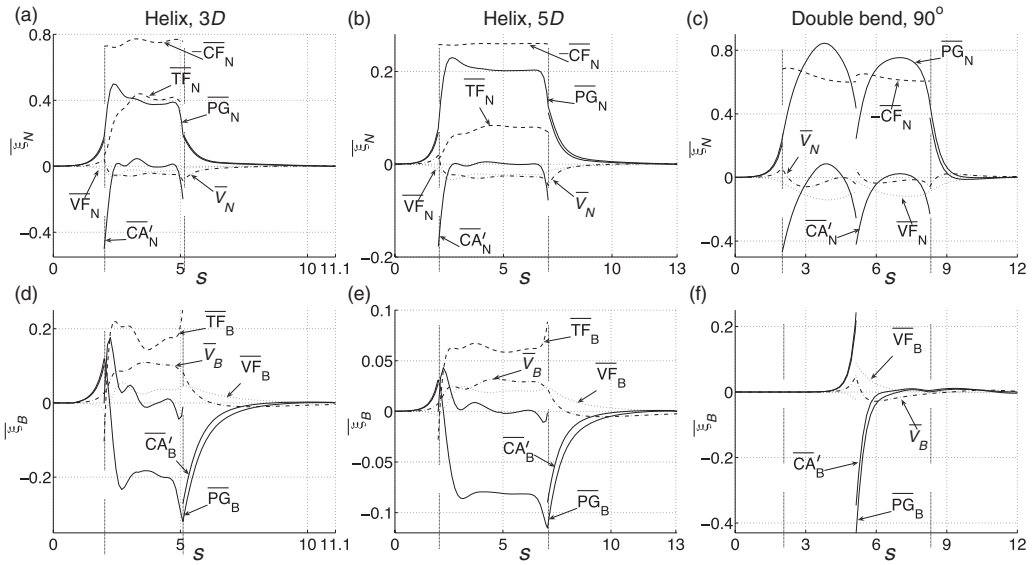

FIG. 10. Cross-sectionally averaged (top) normal acceleration $\overline{\mathrm{CA}'_N}$, forces per unit of mass $-\overline{\mathrm{CF}_N}$, $\overline{\mathrm{TF}_N}$, $\overline{\mathrm{PG}_N}$, and $\overline{\mathrm{VF}_N}$, and velocity $\overline{V_N}$, and (bottom) binormal acceleration $\overline{\mathrm{CA}'_B}$, forces per unit of mass $\overline{\mathrm{TF}_B}$, $\overline{\mathrm{PG}_B}$, and $\overline{\mathrm{VF}_B}$, and velocity $\overline{V_B}$ for $Re = 125$ along the centreline of the helical bends with a pitch length of (left) $3D$ and (middle) $5D$, and (right) the double bend with a 90° azimuthal angle (Figs. 1(a) and 1(b)). Note that $-\mathrm{CF}_N$ is centripetal. The dashed vertical lines indicate the start and end of the curved regions.

oscillators are coupled through $\overline{\mathrm{TF}_N}$ and $\overline{\mathrm{TF}_B}$, which are, respectively, proportional to $\overline{V_B}$ and $\overline{V_N}$ (Eq. (17)).

As the Reynolds number Re increases, the balance between the normal and binormal inertial forces and the corresponding pressure gradients produces greater oscillations of $\overline{\mathrm{CA}'_N}$ and $\overline{\mathrm{CA}'_B}$ around the fully developed state (Fig. 8). Therefore, it takes a longer distance for $\overline{\mathrm{PG}_N}$ and $\overline{\mathrm{PG}_B}$ to reach the fully developed (equilibrium) state.

C. Effect of the centrifugal and torsional forces on axial flows

Secondary motions have an important effect on the axial balance of momentum. The bulk of the axial flow is driven by the axial pressure gradient, PG_s, which is greater in the inner core within most of the curved regions (Figs. 4(q) and 4(r) and 6(q) and 6(r)). This is due to the greater rate of decrease of the pressure at the inner wall as s increases (Fig. 4(w)) that is required to have an in-plane PG opposing the centrifugal force CF_N.

About $1D$ before entering a curve, the uniform PG_s and zero in-plane PG of Poiseuille flow evolve into the patterns obtained at the start of the curve (Figs. 4(i) and 4(q) and 6(i) and 6(q)). The in-plane PG displaces fluid particles toward the inner core, where PG_s yields greater accelerations. Therefore, the position of the peak axial velocity moves toward the inner bend (Figs. 4(a), 6(a), 11(d), and 11(e)); toward the (**N**,**B**)–quadrant in helices (Fig. 6(a)) due to the asymmetric pressure gradients introduced by the torsional force, TF. In planar bends, this is in agreement with experimental observations.[13]

Before the curve ends, there is a greater rate of decrease of the pressure at the outer wall as s increases (e.g., see Fig. 4(w) from $s = 8D$ to $10D$) to lower $\overline{\mathrm{PG}_N}$ in anticipation of the disappearance of CF_N. Thus, PG_s is greater in the outer core (Figs. 4(s) and 6(s)) which, combined with the growing centrifugal $\overline{\mathrm{CA}'_N}$ (Figs. 8, 10(a), and 10(b)), displaces the position of the peak axial velocity centrifugally (Figs. 11(d) and 11(e)); toward the (-**N**,**B**)–quadrant in helices (Fig. 6(c)) due to the effect of TF.

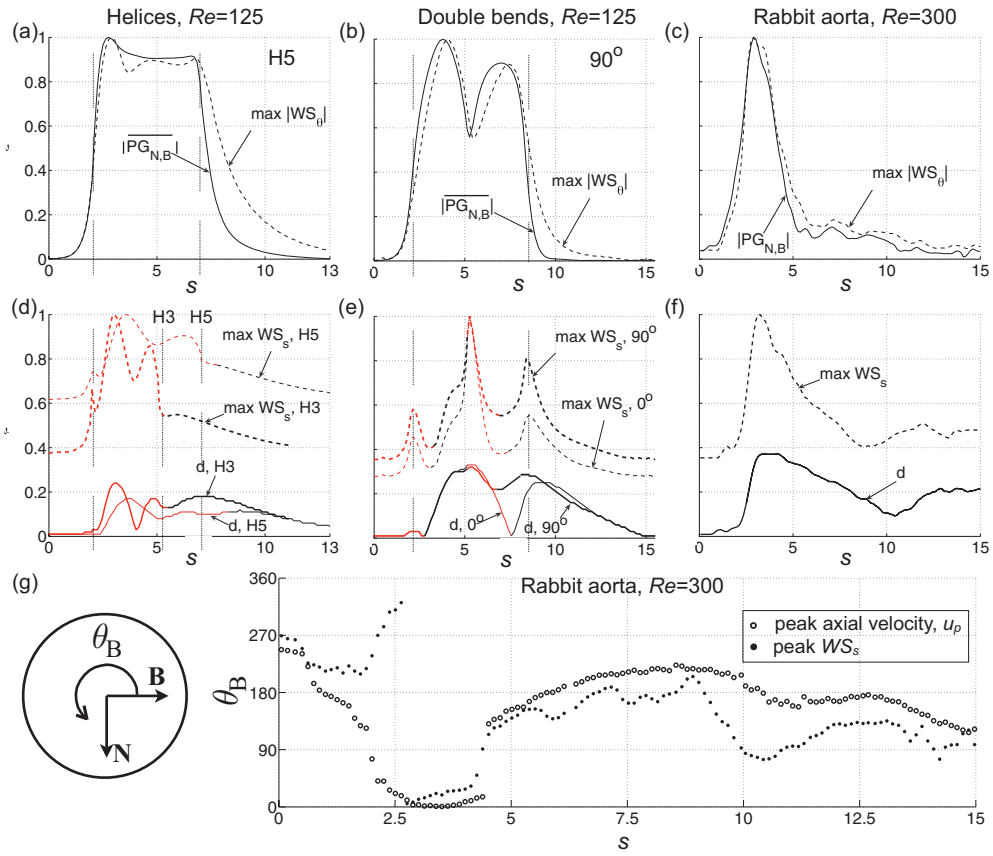

FIG. 11. (Top) Modulus $|\overline{\mathrm{PG}_{N,B}}|$ of the averaged normal and binormal pressure gradients, calculated as $\sqrt{(\overline{\mathrm{PG}_N})^2+(\overline{\mathrm{PG}_B})^2}$, and maximum magnitude of the circumferential WSS, $|WS_\theta|$, with s in the (a) helical bend with a pitch length of $5D$, (b) double bend with a 90° azimuthal angle, and (c) rabbit aorta (Fig. 1). (Middle) Radial offset, d, of the position of the peak axial velocity, u_p, measured from the vessel centreline, and maximum axial WSS, WS_s, with s in the (d) helical bends with pitch lengths of $3D$ (H3) and $5D$ (H5), (e) double bends with 0° and 90° azimuthal angles, and (f) rabbit aorta. (g) Circumferential angle θ_B, measured from **B**, of the location of u_p (circles) and the maximum WS_s (dots) for the rabbit aorta. Wall stresses and $|\overline{\mathrm{PG}_{N,B}}|$ are non-dimensionalised by their corresponding maximum values. Offsets d are non-dimensionalised by the pipe diameter D. For panels (d) and (e), maximum WS_s at the inner wall and d with u_p in the inner core are shown in light grey lines (red online). The dashed vertical lines indicate the start and end of the curved regions.

1. The role of the full Coriolis force 2Co

According to Eq. (12), the full Coriolis force, 2Co, accelerates downstream fluid particles with a centripetal normal velocity (i.e., $V_N > 0$) and vice versa ($\Omega > 0$ for any s since the axial flow does not reverse; i.e., $u > 0$). Thus, 2Co accelerates the bulk of the flow at the start of the single bend and helix (Figs. 4(o) and 6(o)) for as long as V_N is predominantly centripetal (i.e., $\overline{V_N} > 0$). This contributes to retain the peak axial velocity in the inner core (Figs. 11(d) and 11(e)).

Moving downstream, the secondary flows developed by the centrifugal and torsional forces lead to profound changes in 2Co, as the change of $\overline{V_N}$ from centripetal to centrifugal (Figs. 8, 10(a), and 10(b)) suggests. The jet-like secondary motions that develop in the core yield a Coriolis deceleration, $2\mathrm{Co} < 0$, while the opposite near-wall flows yield a Coriolis acceleration, $2\mathrm{Co} > 0$ (Figs. 4(p) and 6(p)). This pattern of 2Co, whose extremes increase with torsion τ and Dean number De, slows the bulk of the flow and stretches its profile circumferentially. Thus, the circular velocity profile at the start of the curves evolves into shapes that are first elliptical and then crescent with increasing s, De, and τ (Figs. 4(a)–4(c), 5(a)–5(e), and 6(a)–6(c)).

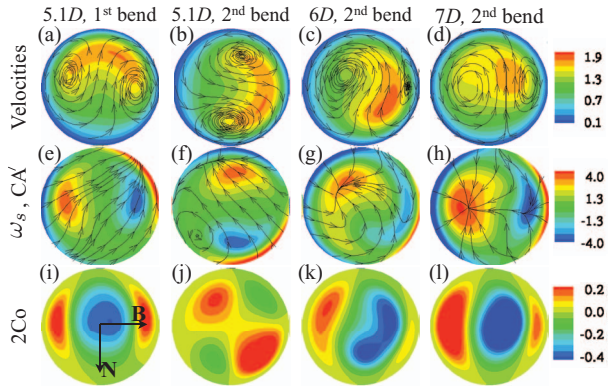

FIG. 12. Contours of axial velocity (top), vorticity (middle), and full Coriolis force per unit of mass, 2Co, (bottom) for $Re = 125$ in the double bend with an azimuthal angle of 90° (Fig. 1(a)), at $s = 5.14D$ in the first bend and $5.14D$, $6D$, and $7D$ in the second bend. The secondary-flow streamlines and directions of the in-plane convective acceleration, CA′, are overlaid within the velocity and vorticity contours, respectively. The local **N** and **B** are oriented as shown in (i).

D. Flow patterns in double bends

The very localised pattern of the cross-sectional averages $\overline{\mathrm{CA}'_B}$, $\overline{\mathrm{PG}_B}$, $\overline{\mathrm{VF}_B}$, and $\overline{V_B}$ in the double bends (Fig. 1(a)) at $s = 5.14D$ (where the plane of curvature changes) is similar to the features observed at the start and the end of the helical regions (Fig. 1(b)), as Figs. 10(d)–10(f) show for the 90° double bend at $Re = 125$. This similarity suggests that we can interpret the mechanisms underlying the flow patterns in double bends by considering an impulse injection of averaged binormal torsional force $\overline{\mathrm{TF}_B} < 0$ at the end of the first bend and $\overline{\mathrm{TF}_B} > 0$ at the start of the second bend.

At the end of the first bend, the core flow is accelerated toward the (-**N**,**B**)–quadrant (Fig. 12(e)). This is due to an increase in $\overline{\mathrm{PG}_B}$ (Fig. 10(f)), which anticipates the impulse injection of $\overline{\mathrm{TF}_B} < 0$, and to a drop in $\overline{\mathrm{PG}_N}$ (Fig. 10(c)), which can be thought of $\overline{\mathrm{PG}_N}$ anticipating about $1D$ upstream $s = 5.14D$ an impulse injection of $\overline{\mathrm{TF}_N} > 0$. Therefore, $\overline{\mathrm{CA}'_N}$ drops and $\overline{\mathrm{CA}'_B}$ increases which, combined with a greater axial pressure gradient, PG_s, in the (-**N**,**B**)–quadrant, skews the bulk of the axial flow toward this quadrant (Fig. 12(a)). This skewing and the extremes of $\overline{\mathrm{PG}_B}$ are maximal for a 90° azimuthal angle between the plane of curvature of each bend.

At the start of the second bend, the full Coriolis force, 2Co, accelerates the bulk of the flow (Fig. 12(j)) within less than $1D$, while $\overline{V_N} > 0$ in Fig. 10(c). This contributes to enhance the velocity profile inherited from the first bend, which has been rotated (Fig. 12(b)) by the impulse torsional force.

The flow develops up to $1D$ before the second bend ends, as indicated by $\overline{\mathrm{CA}'_N}$, $\overline{\mathrm{CA}'_B}$, $\overline{V_N}$, and $\overline{V_B}$ approaching zero (Figs. 10(c) and 10(f)). As s increases, the pressure gradient accelerates the core flow toward the (**N**, -**B**)–quadrant to oppose the centrifugal force and rotate the position of the core vortices anticlockwise, restoring the axisymmetry of the secondary flow (Figs. 12(f)–12(h)). Thus, $\overline{\mathrm{PG}_N}$ grows to oppose $\overline{\mathrm{CF}_N}$ and bring $\overline{\mathrm{CA}'_N}$ to zero, and $\overline{\mathrm{PG}_B}$ is negative. Flow axisymmetry is also restored by the full Coriolis force, 2Co, which stretches the bulk of the axial flow anticlockwise (Figs. 12(k) and 12(l)).

With decreasing azimuthal angle in Fig. 1(a), $\overline{\mathrm{PG}_N}$ and $\overline{\mathrm{CA}'_N}$ drop at the end of the first bend and the start of the second, and the centripetal force, $-\overline{\mathrm{CF}_N}$, increases in the second bend (Figs. 13(a)–13(c)). For the 45° and 0° cases, $\overline{\mathrm{PG}_N}$ is centrifugal in the second bend (Fig. 13(a)) to decelerate, together with $\overline{\mathrm{CF}_N}$, centripetal secondary motions inherited from the first bend, which grow with decreasing azimuthal angle (Fig. 13(d)). The evolution of these averages indicates a stronger flow coupling across the two bends with decreasing azimuthal angle, offering an alternative method to the λ_2 iso-contours[25,31] for quantifying and comparing the strength of this coupling for different angles and Re.

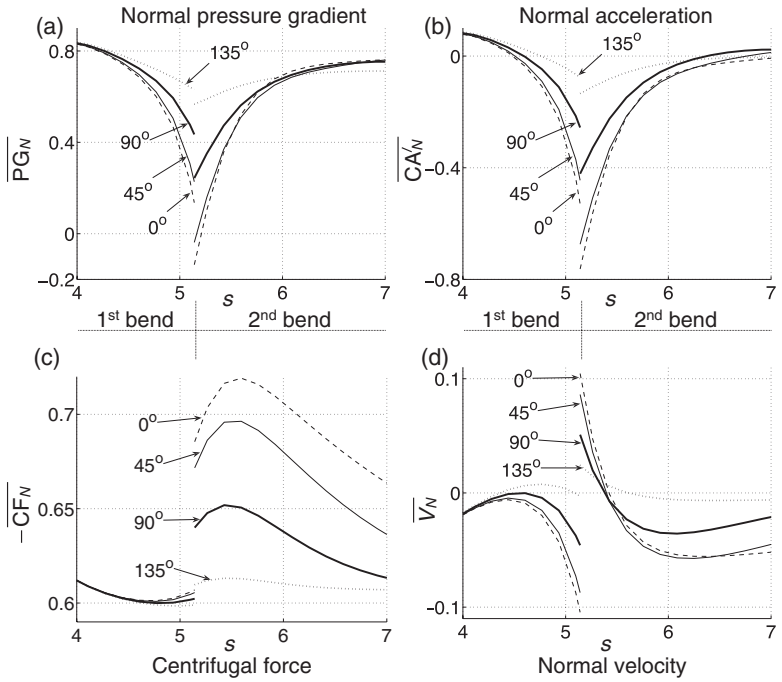

FIG. 13. Cross-sectionally averaged normal (a) pressure gradient, $\overline{\mathrm{PG}_N}$, (b) convective acceleration, $\overline{\mathrm{CA}'_N}$, (c) centripetal force, $-\overline{\mathrm{CF}_N}$, and (d) velocity, $\overline{V_N}$, at $Re = 125$ around $s = (2 + \pi)D$ (where the plane of curvature changes) in the double bends (Fig. 1(a)). The labels indicate the azimuthal angles between the plane of curvature of each bend.

E. Flow patterns in an image-based rabbit thoracic aorta

As in the helices, the dominant normal driving force of the secondary flows in the rabbit thoracic aorta (Figs. 1(c) and 14(c)) is the centrifugal force, CF_N (Fig. 14(d)), despite torsion τ being of the same order as curvature κ along the centreline (τ is even larger than κ in the descending aorta) (Fig. 14(f)). This is because the torsional force, TF, depends on the secondary velocities generated by CF_N, as we described in Sec. IV B 2. Note that the averaged normal, $\overline{\mathrm{TF}_N}$, and binormal, $\overline{\mathrm{TF}_B}$, torsional forces are about one order of magnitude smaller than $\overline{\mathrm{CF}_N}$ in the first part of the aortic arch and negligible from about $s > 6D$, despite τ reaching its extreme values for $s > 6D$ (Figs. 14(d)–14(f)). The smooth changes in κ with s allow $\overline{\mathrm{PG}_N}$ to counterbalance $\overline{\mathrm{CF}_N}$ generating a relatively smaller and more uniform averaged acceleration $\overline{\mathrm{CA}'_N}$ than in previous geometries and, hence, a relatively smaller averaged velocity $\overline{V_N}$. As in the previous geometries, the directions of in-plane CA' tend to point toward the centres of vortices (Figs. 14(m)–14(o)).

In the ascending aorta, the interaction between CF_N and the opposing in-plane PG forms a pair of counter-rotating (Dean-type) vortices. The flow symmetry is broken by the torsional force, TF, which expands the vortex of positive ω_s and accelerates the core flow in the direction of **B** up to $s = 4D$ (as indicated by $\overline{\mathrm{TF}_B} > 0$ in Fig. 14(e)); the directions of TF are similar to those shown in Fig. 14(j) at $s = 3D$. As in the helices, TF rotates clockwise the positions of the two vortices (Fig. 14(m)) and yields asymmetric pressure gradients that rotate clockwise the bulk of the axial flow (Fig. 14(g)).

In the second half of the aortic arch, the positions of the two vortices rotate anticlockwise. The vortex of positive ω_s moves toward the centre of the cross section (Fig. 14(n)) generating a dominant anticlockwise swirling flow (Fig. 14(h)). From the end of the arch, TF (Figs. 14(k) and 14(l)) helps to recover flow axisymmetry in the descending aorta (Figs. 14(i) and 14(o)) by expanding the vortex of negative ω_s and contracting that of positive ω_s.

The full Coriolis force, 2Co, stretches the bulk of the axial flow in the aortic arch (Figs. 14(p)–14(r)). As curvature κ drops with s, 2Co decreases in magnitude and is overpowered by the axial

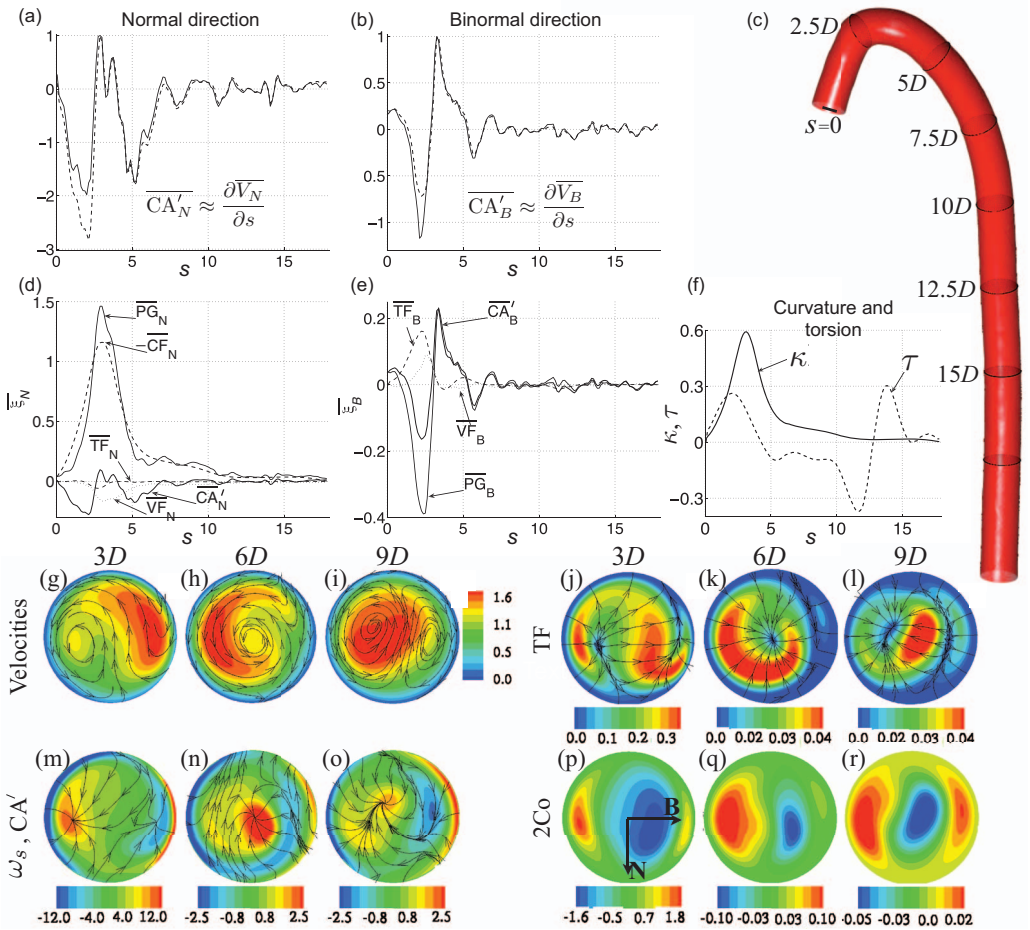

FIG. 14. Centreline results in the rabbit thoracic aorta in (c) with the curvature and torsion in (f) and $Re = 300$: (top, (a) and (b)) Cross-sectional averages $\overline{\mathrm{CA}'_N}$, $\overline{\mathrm{CA}'_B}$ (dashed lines), $\frac{\partial \overline{V_N}}{\partial s}$, and $\frac{\partial \overline{V_B}}{\partial s}$ (solid lines) along the centreline non-dimensionalised by their corresponding maximum values. (Middle) Cross-sectionally averaged normal (d) and binormal (e) accelerations and forces per unit of mass along the centreline. (Bottom) Magnitude contours of the following local quantities at $s = 3D$, $6D$, and $9D$: axial velocity with secondary-flow streamlines (g)–(i), torsional force per unit of mass, TF, with its directions overlaid (j)–(l), axial vorticity, ω_s, with overlaid directions of the in-plane convective acceleration, CA′, (m)–(o), and full Coriolis force per unit of mass, 2Co, (p)–(r). The local **N** and **B** are oriented as shown in (p).

viscous force, VF_s, which gradually transforms the axial velocity profile into a circular shape in the descending aorta (Fig. 14(i)).

F. Wall stresses

All the geometries studied show a good correlation between the evolutions with s of the modulus $\sqrt{(\overline{\mathrm{PG}_N})^2+(\overline{\mathrm{PG}_B})^2}$ of the normal and binormal pressure gradients, PG, and the maximum magnitude of the circumferential WSS, $|WS_\theta|$ (Figs. 11(a)–11(c)), and, hence, the maximum generation of wall axial vorticity ω_s; see Eq. (24). This is because the greater the in-plane PG, the faster it drives near-wall fluid particles, producing greater $|WS_\theta|$. This correlation is in agreement with the averaged normal, $\overline{\mathrm{VF}_N}$, and binormal, $\overline{\mathrm{VF}_B}$, viscous forces being approximately proportional to $-\overline{\mathrm{PG}_N}$ and $-\overline{\mathrm{PG}_B}$, respectively (Figs. 8, 10, 14(d), and 14(e)), and the locations on the wall of the extremes of the in-plane viscous force, VF, coinciding with those of the circumferential wall traction, $-WS_\theta$ (Figs. 4(l)–4(n), 4(x), 6(l)–6(n), and 6(w)).

Moreover, the radial offset, d, of the position of the peak axial velocity, u_p, correlates well with the maximum axial WSS, WS_s, in each cross section (Figs. 11(d)–11(f)). The circumferential angles

where u_p and the maximum WS_s occur are also similar; e.g., see Fig. 11(g) for the rabbit aorta. For the helices and double bends, Figs. 11(d) and 11(e) show that the maximum WS_s alternates between the inner (highlighted in light grey lines; red online) and outer sides with s, at about the same points as does d. This is because a greater d yields greater velocity gradients $\frac{\partial u}{\partial r}$ at the wall next to where u_p is attained. According to Eq. (23), greater tractions $-WS_s$ occur (Figs. 4(y) and 6(x)) which, together with the axial viscous force, VF_s (Figs. 4(t)–4(v) and 6(t)–6(v)), push the bulk of the flow away from the wall.

We can use these two correlations to describe mechanisms underlying the effect of curvature κ and torsion τ on the evolution of the maximum $|WS_\theta|$ and WS_s with s. For example, comparison of WS_θ for the single bend with $\kappa = 0.5/D$ and for the helical bend with $\kappa = 0.51/D$ in Figs. 4(x) and 6(w) shows that τ leads to more uniform WS_θ. This is because the centripetal $\overline{\mathrm{TF}_N}$ reduces the centripetal $\overline{\mathrm{PG}_N}$ required to counteract the centrifugal $\overline{\mathrm{CF}_N}$, leading to smaller $\sqrt{(\overline{\mathrm{PG}_N})^2+(\overline{\mathrm{PG}_B})^2}$ in the helix (despite the nonzero $\overline{\mathrm{PG}_B}$) and, hence, smaller $|WS_\theta|$.

At the entrance of the planar bends, the extremes of WS_s swap from the inner to the outer wall (Fig. 4(y)), due to the change in the sign of the radial offset d (Fig. 11(e)). The crossover occurs closer to the bend inlet as Re increases, in line with experimental results.[40,41] In double bends, the crossover occurs further downstream in the second bend as the azimuthal angle decreases, since it takes CF_N longer to move the bulk of the flow from the inner to the outer cores (Fig. 11(e)). In fact, the peak WS_s at the start of the second bend increases with decreasing azimuthal angle (Fig. 11(e)), indicating a stronger wall reaction to maintain the bulk of the flow off the inner wall.

As the inertial forces vanish, wall stresses gradually evolve into the zero WS_θ and uniform WS_s and wall pressure of Poiseuille flow (Figs. 4(w)–4(y) and 11(a)–11(f)). As $|WS_\theta|$ drops, the wall generates less axial vorticity, ω_s (Eq. (24), Figs. 4(f) and 6(f)). In the core flow, ω_s is dissipated by the in-plane VF (Figs. 4(n) and 6(n)).

V. CONCLUSIONS AND PHYSIOLOGICAL IMPLICATIONS

We have investigated the mechanisms by which vascular curvature and torsion affect blood flow patterns and wall stresses. By calculating forces and accelerations in an orthogonal coordinate system following the vessel centreline, we have separated the individual roles of the inertial forces, which explicitly depend on the curvature and torsion of the centreline, pressure gradient, and viscous forces. By taking cross-sectional averages of their components in the local normal and binormal directions, we have described how these forces interact along the centreline, changing the location and magnitude of the peak axial velocity and the maximum wall shear stresses. We have applied our new method to study Newtonian fluids in pipes with rigid walls, which are assumptions that replicate the dominant features of large-artery flows.[42,43]

Application of our method to geometries with idealised and anatomically realistic curvature and torsion has shown that, for $Re \in [50, 500]$, the averaged normal and binormal forces mainly govern the averaged motions in each corresponding direction (Figs. 7, 14(a), and 14(b)). These motions oscillate around the fully developed state; the equilibrium state in which averaged normal and binormal accelerations are zero. The amplitudes of these oscillations are greater with increasing Dean number and torsion. This observation has allowed us to assign physical roles to averaged forces, based on the forces acting in underdamped oscillators, as follows. The centrifugal and torsional forces drive secondary motions. The centrifugal force generates motions in the normal direction from motions in the axial direction, whereas the torsional force couples normal and binormal motions. The normal and binormal pressure gradients are restoring forces that react to the in-plane inertial forces to maintain the flow within the pipe and bring the flow to the fully developed (equilibrium) state. The "frictional" viscous forces primarily oppose the in-plane pressure gradients, rather than the inertial forces.

The torsional force is associated with non-planarity and depends on the secondary motions generated by the curvature-dependent centrifugal force. It breaks the symmetry of the flow and has a profound effect on flow mixing and the distributions of WSS, which are important properties for the effective design of vascular prostheses and surgical reconstructions.[7] The torsional force makes one vortex dominant, which, according to Ref. 23 enhances in-plane mixing through stirring. In double

bends, similar vortical structures are formed by non-planarity, which can be thought of introducing an impulse torsional force. This force yields maximum averaged binormal accelerations for an azimuthal angle of 90°, which suggests that this is the optimal angle to increase flow asymmetry and, therefore, provide enhanced mixing.

According to Ref. 7, torsion protects from vessel occlusion by generating a more uniform spatial distribution of WSS. However, only the circumferential WSS becomes more uniform in our helical bend with the same curvature as our single bend. Thus, it seems there is an optimal value of torsion to regularise the distribution of WSS.

Secondary motions directly affect the axial balance of momentum. The non-uniform wall pressures arising to counterbalance the inertial forces result in non-uniform axial pressure gradients, whose accelerations, combined with the in-plane accelerations, radially displace the position of the peak axial velocity. This alternates between the inner and outer cores along the pipe. The curvature-dependent Coriolis force directly links motions in the normal direction to axial accelerations: it enhances the bulk of the axial flow if secondary motions are predominantly centripetal, and vice versa. As the flow develops, the Coriolis force shapes the velocity profile, from circular to crescent shapes. This force also helps restore flow axisymmetry where torsion is absent.

Reduction of the dynamics of secondary flows onto the vessel centreline also allows us to study the mechanisms by which vascular curvature and torsion affect the evolution of the maximum WSS along the pipe. This can be achieved since the maximum axial and circumferential WSS correlate well with the radial offset of the peak axial velocity and the averaged in-plane normal and binormal pressure gradients, respectively. Moreover, these correlations can provide valuable insight into estimating the positions of the extremes of WSSs along the pipe from *in vivo* 3D flow data.

We have demonstrated that changes in curvature and torsion affect in-plane accelerations at least one diameter upstream and downstream, since the in-plane pressure gradient gradually anticipates changes in the in-plane inertial forces. Thus, the pressure and velocity fields are smooth despite abrupt changes in the inertial forces. Upstream and downstream transmissions of geometric changes via pressure variations show the elliptical character of the Navier–Stokes equations.

With our analysis we can quantify the level of flow development within finite-length bends with approximately constant curvature and torsion. Thus, asymptotic solutions for fully developed flow are less valid in regions with relatively large averaged normal and binormal accelerations. We can also quantify the level of flow coupling across adjacent bends. Effects that have yet to be explored include tapering, non-circular lumina, branching, unsteady flows, non-Newtonian fluid behaviour, and more realistic boundary conditions. Non-circular lumina can also be analysed with the current formulation, since the mapping from Cartesian to local coordinates only depends on the geometry of the centreline. Temporal accelerations are also straightforward to include in our analysis, since they are not affected by the transformation from Cartesian to local coordinates. Application of our analysis to pulsatile flows is likely to enhance our understanding of the role of vessel curvature and torsion on the one-dimensional modelling of pulse wave propagation,[44,45] in particular, on the energy losses they introduce.

Our use of a decomposition of local momentum into components following the vessel centreline allows us to gain more insight into mechanisms underlying the effect of vascular bending and twisting on the flow and wall stresses. It could also help in understanding fluid dynamics in other physiological and industrial curved pipes, such as airways and heat exchangers.

ACKNOWLEDGMENTS

The authors are very grateful to Dr. Dana Lee for providing the Cartesian velocity and pressure gradient fields of the idealised geometries and Dr. Luca Antiga for fruitful discussions. This research was supported by an EPSRC Advanced Research Fellowship, EP/C539834/1, and associated grant, EP/C539842/1. Jordi Alastruey gratefully acknowledges the support of a British Heart Foundation (BHF) Intermediate Basic Science Research Fellowship (FS/09/030/27812) and the Centre of Excellence in Medical Engineering funded by the Wellcome Trust and EPSRC under Grant No. WT 088641/Z/09/Z. Véronique Peiffer is funded by the BHF Centre of Research Excellence at Imperial College London.

APPENDIX: VELOCITY AND PRESSURE GRADIENTS: FROM CARTESIAN TO LOCAL COORDINATES

Given the velocity vector $\tilde{\mathbf{V}} = (\tilde{u}, \tilde{v}, \tilde{w})$ in Cartesian coordinates (x, y, z), we can determine $\mathbf{V} = (u, v, w)$ in local coordinates (s, r, θ) by projecting $\tilde{\mathbf{V}}$ onto the directions $\mathbf{a}_s$, $\mathbf{a}_r$, and $\mathbf{a}_\theta$,

$$u = \tilde{\mathbf{V}} \cdot \mathbf{a}_s, \quad v = \tilde{\mathbf{V}} \cdot \mathbf{a}_r, \quad w = \tilde{\mathbf{V}} \cdot \mathbf{a}_\theta. \tag{A1}$$

Differentiation of Eqs. (A1) using the relations in Eqs. (1) and (2) allows us to calculate the first and second partial derivatives of u, v, w in local coordinates from the corresponding derivatives in Cartesian coordinates. The first partial derivatives take the form

$$\frac{\partial u}{\partial s} = \frac{\partial \tilde{\mathbf{V}}}{\partial s} \cdot \mathbf{T} + \kappa \tilde{\mathbf{V}} \cdot \mathbf{N}, \qquad \frac{\partial u}{\partial r} = \frac{\partial \tilde{\mathbf{V}}}{\partial r} \cdot \mathbf{T}, \qquad \frac{\partial u}{\partial \theta} = \frac{\partial \tilde{\mathbf{V}}}{\partial \theta} \cdot \mathbf{T},$$

$$\frac{\partial v}{\partial s} = \frac{\partial \tilde{\mathbf{V}}}{\partial s} \cdot \mathbf{a}_r + \kappa \sin(\theta + \phi) \tilde{\mathbf{V}} \cdot \mathbf{T}, \qquad \frac{\partial v}{\partial r} = \frac{\partial \tilde{\mathbf{V}}}{\partial r} \cdot \mathbf{a}_r, \qquad \frac{\partial v}{\partial \theta} = \frac{\partial \tilde{\mathbf{V}}}{\partial \theta} \cdot \mathbf{a}_r + \tilde{\mathbf{V}} \cdot \mathbf{a}_\theta,$$

$$\frac{\partial w}{\partial s} = \frac{\partial \tilde{\mathbf{V}}}{\partial s} \cdot \mathbf{a}_\theta + \kappa \cos(\theta + \phi) \tilde{\mathbf{V}} \cdot \mathbf{T}, \qquad \frac{\partial w}{\partial r} = \frac{\partial \tilde{\mathbf{V}}}{\partial r} \cdot \mathbf{a}_\theta, \qquad \frac{\partial w}{\partial \theta} = \frac{\partial \tilde{\mathbf{V}}}{\partial \theta} \cdot \mathbf{a}_\theta - \tilde{\mathbf{V}} \cdot \mathbf{a}_r,$$

where $\frac{\partial \tilde{\mathbf{V}}}{\partial s}$, $\frac{\partial \tilde{\mathbf{V}}}{\partial r}$, and $\frac{\partial \tilde{\mathbf{V}}}{\partial \theta}$ are related to the Cartesian partial derivatives of $\tilde{u}$, $\tilde{v}$, and $\tilde{w}$ through the chain rule; i.e.,

$$\frac{\partial \tilde{\mathbf{V}}}{\partial s} = \mathbf{J} \frac{\partial \mathbf{x}}{\partial s}, \qquad \frac{\partial \tilde{\mathbf{V}}}{\partial r} = \mathbf{J} \frac{\partial \mathbf{x}}{\partial r}, \qquad \frac{\partial \tilde{\mathbf{V}}}{\partial \theta} = \mathbf{J} \frac{\partial \mathbf{x}}{\partial \theta},$$

with

$$\frac{\partial \mathbf{x}}{\partial s} = h\mathbf{T}, \quad \frac{\partial \mathbf{x}}{\partial r} = \mathbf{a}_r, \quad \frac{\partial \mathbf{x}}{\partial \theta} = r\mathbf{a}_\theta, \qquad \mathbf{J} = \begin{bmatrix} \frac{\partial \tilde{u}}{\partial x} & \frac{\partial \tilde{u}}{\partial y} & \frac{\partial \tilde{u}}{\partial z} \\ \frac{\partial \tilde{v}}{\partial x} & \frac{\partial \tilde{v}}{\partial y} & \frac{\partial \tilde{v}}{\partial z} \\ \frac{\partial \tilde{w}}{\partial x} & \frac{\partial \tilde{w}}{\partial y} & \frac{\partial \tilde{w}}{\partial z} \end{bmatrix} = \begin{bmatrix} \mathbf{J}_{\tilde{\mathbf{u}}} \\ \mathbf{J}_{\tilde{\mathbf{v}}} \\ \mathbf{J}_{\tilde{\mathbf{w}}} \end{bmatrix}. \tag{A2}$$

The second partial derivatives take the form

$$\frac{\partial^2 u}{\partial s^2} = \frac{\partial^2 \tilde{\mathbf{V}}}{\partial s^2} \cdot \mathbf{T} + 2\kappa \frac{\partial \tilde{\mathbf{V}}}{\partial s} \cdot \mathbf{N} + \kappa \tilde{\mathbf{V}} \cdot (\tau \mathbf{B} - \kappa \mathbf{T}) + \frac{\mathrm{d}\kappa}{\mathrm{d}s} \tilde{\mathbf{V}} \cdot \mathbf{N},$$

$$\frac{\partial^2 u}{\partial r^2} = \frac{\partial^2 \tilde{\mathbf{V}}}{\partial r^2} \cdot \mathbf{T}, \qquad \frac{\partial^2 u}{\partial \theta^2} = \frac{\partial^2 \tilde{\mathbf{V}}}{\partial \theta^2} \cdot \mathbf{T},$$

$$\frac{\partial^2 u}{\partial s \partial r} = \frac{\partial^2 \tilde{\mathbf{V}}}{\partial s \partial r} \cdot \mathbf{T} + \kappa \frac{\partial \tilde{\mathbf{V}}}{\partial r} \cdot \mathbf{N}, \qquad \frac{\partial^2 u}{\partial r \partial \theta} = \frac{\partial^2 \tilde{\mathbf{V}}}{\partial r \partial \theta} \cdot \mathbf{T},$$

$$\frac{\partial^2 u}{\partial \theta \partial s} = \frac{\partial^2 \tilde{\mathbf{V}}}{\partial \theta \partial s} \cdot \mathbf{T} + \kappa \frac{\partial \tilde{\mathbf{V}}}{\partial \theta} \cdot \mathbf{N},$$

$$\frac{\partial^2 v}{\partial s^2} = \frac{\partial^2 \tilde{\mathbf{V}}}{\partial s^2} \cdot \mathbf{a}_r + 2\kappa \sin(\theta + \phi) \frac{\partial \tilde{\mathbf{V}}}{\partial s} \cdot \mathbf{T} + \left[\frac{\mathrm{d}\kappa}{\mathrm{d}s} \sin(\theta + \phi) - \tau\kappa \cos(\theta + \phi) \right] \tilde{\mathbf{V}} \cdot \mathbf{T} + \kappa^2 \sin(\theta + \phi) \tilde{\mathbf{V}} \cdot \mathbf{N},$$

$$\frac{\partial^2 v}{\partial r^2} = \frac{\partial^2 \tilde{\mathbf{V}}}{\partial r^2} \cdot \mathbf{a}_r, \qquad \frac{\partial^2 v}{\partial \theta^2} = \frac{\partial^2 \tilde{\mathbf{V}}}{\partial \theta^2} \cdot \mathbf{a}_r + 2 \frac{\partial \tilde{\mathbf{V}}}{\partial \theta} \cdot \mathbf{a}_\theta - \tilde{\mathbf{V}} \cdot \mathbf{a}_r,$$

$$\frac{\partial^2 v}{\partial s \partial r} = \frac{\partial^2 \tilde{\mathbf{V}}}{\partial s \partial r} \cdot \mathbf{a}_r + \kappa \sin(\theta + \phi) \frac{\partial \tilde{\mathbf{V}}}{\partial r} \cdot \mathbf{T}, \quad \frac{\partial^2 v}{\partial r \partial \theta} = \frac{\partial^2 \tilde{\mathbf{V}}}{\partial r \partial \theta} \cdot \mathbf{a}_r + \frac{\partial \tilde{\mathbf{V}}}{\partial r} \cdot \mathbf{a}_\theta,$$

$$\frac{\partial^2 v}{\partial\theta\partial s} = \frac{\partial^2\tilde{\mathbf{V}}}{\partial\theta\partial s}\cdot\mathbf{a}_r + \frac{\partial\tilde{\mathbf{V}}}{\partial s}\cdot\mathbf{a}_\theta + \kappa\left[\cos(\theta+\phi)\tilde{\mathbf{V}} + \sin(\theta+\phi)\frac{\partial\tilde{\mathbf{V}}}{\partial\theta}\right]\cdot\mathbf{T},$$

$$\frac{\partial^2 w}{\partial s^2} = \frac{\partial^2\tilde{\mathbf{V}}}{\partial s^2}\cdot\mathbf{a}_\theta + 2\kappa\cos(\theta+\phi)\frac{\partial\tilde{\mathbf{V}}}{\partial s}\cdot\mathbf{T} + \left[\frac{\mathrm{d}\kappa}{\mathrm{d}s}\cos(\theta+\phi) + \tau\kappa\sin(\theta+\phi)\right]\tilde{\mathbf{V}}\cdot\mathbf{T} + \kappa^2\cos(\theta+\phi)\tilde{\mathbf{V}}\cdot\mathbf{N},$$

$$\frac{\partial^2 w}{\partial r^2} = \frac{\partial^2\tilde{\mathbf{V}}}{\partial r^2}\cdot\mathbf{a}_\theta,\quad \frac{\partial^2 w}{\partial\theta^2} = \frac{\partial^2\tilde{\mathbf{V}}}{\partial\theta^2}\cdot\mathbf{a}_\theta - 2\frac{\partial\tilde{\mathbf{V}}}{\partial\theta}\cdot\mathbf{a}_r - \tilde{\mathbf{V}}\cdot\mathbf{a}_\theta,$$

$$\frac{\partial^2 w}{\partial s\partial r} = \frac{\partial^2\tilde{\mathbf{V}}}{\partial s\partial r}\cdot\mathbf{a}_\theta + \kappa\cos(\theta+\phi)\frac{\partial\tilde{\mathbf{V}}}{\partial r}\cdot\mathbf{T},\qquad \frac{\partial^2 w}{\partial r\partial\theta} = \frac{\partial^2\tilde{\mathbf{V}}}{\partial r\partial\theta}\cdot\mathbf{a}_\theta - \frac{\partial\tilde{\mathbf{V}}}{\partial r}\cdot\mathbf{a}_r,$$

$$\frac{\partial^2 w}{\partial\theta\partial s} = \frac{\partial^2\tilde{\mathbf{V}}}{\partial\theta\partial s}\cdot\mathbf{a}_\theta - \frac{\partial\tilde{\mathbf{V}}}{\partial s}\cdot\mathbf{a}_r + \kappa\left[-\sin(\theta+\phi)\tilde{\mathbf{V}} + \cos(\theta+\phi)\frac{\partial\tilde{\mathbf{V}}}{\partial\theta}\right]\cdot\mathbf{T},$$

where the second partial derivatives of $\tilde{\mathbf{V}}$ in local coordinates are related to the Cartesian first and second partial derivatives of $\tilde{u}$, $\tilde{v}$, and $\tilde{w}$ through the chain rule; i.e.,

$$\frac{\partial^2\tilde{u}}{\partial i\partial j} = \left[\frac{\partial\mathbf{x}}{\partial i}\right]^{\mathrm{T}}\mathbf{H}_{\tilde{u}}\frac{\partial\mathbf{x}}{\partial j} + \mathbf{J}_{\tilde{\mathbf{u}}}\frac{\partial^2\mathbf{x}}{\partial i\partial j},\qquad \frac{\partial^2\tilde{v}}{\partial i\partial j} = \left[\frac{\partial\mathbf{x}}{\partial i}\right]^{\mathrm{T}}\mathbf{H}_{\tilde{v}}\frac{\partial\mathbf{x}}{\partial j} + \mathbf{J}_{\tilde{\mathbf{v}}}\frac{\partial^2\mathbf{x}}{\partial i\partial j},$$

$$\frac{\partial^2\tilde{w}}{\partial i\partial j} = \left[\frac{\partial\mathbf{x}}{\partial i}\right]^{\mathrm{T}}\mathbf{H}_{\tilde{w}}\frac{\partial\mathbf{x}}{\partial j} + \mathbf{J}_{\tilde{\mathbf{w}}}\frac{\partial^2\mathbf{x}}{\partial i\partial j},\qquad i,j = s,r,\theta,$$

with

$$\frac{\partial^2\mathbf{x}}{\partial s^2} = \left[\frac{\mathrm{d}\kappa}{\mathrm{d}s}r\sin(\theta+\phi) - \tau\kappa r\cos(\theta+\phi)\right]\mathbf{T} + h\kappa\mathbf{N},\qquad \frac{\partial^2\mathbf{x}}{\partial r^2} = \mathbf{0},\qquad \frac{\partial^2\mathbf{x}}{\partial\theta^2} = -r\mathbf{a}_r,$$

$$\frac{\partial^2\mathbf{x}}{\partial s\partial r} = \kappa\sin(\theta+\phi)\mathbf{T},\qquad \frac{\partial^2\mathbf{x}}{\partial r\partial\theta} = \mathbf{a}_\theta,\qquad \frac{\partial^2\mathbf{x}}{\partial\theta\partial s} = \kappa r\cos(\theta+\phi)\mathbf{T},$$

$$\mathbf{H}_{\tilde{u}} = \begin{bmatrix} \frac{\partial^2\tilde{u}}{\partial x^2} & \frac{\partial^2\tilde{u}}{\partial x\partial y} & \frac{\partial^2\tilde{u}}{\partial x\partial z} \\ \frac{\partial^2\tilde{u}}{\partial y\partial x} & \frac{\partial^2\tilde{u}}{\partial y^2} & \frac{\partial^2\tilde{u}}{\partial y\partial z} \\ \frac{\partial^2\tilde{u}}{\partial z\partial x} & \frac{\partial^2\tilde{u}}{\partial z\partial y} & \frac{\partial^2\tilde{u}}{\partial z^2} \end{bmatrix},\ \mathbf{H}_{\tilde{v}} = \begin{bmatrix} \frac{\partial^2\tilde{v}}{\partial x^2} & \frac{\partial^2\tilde{v}}{\partial x\partial y} & \frac{\partial^2\tilde{v}}{\partial x\partial z} \\ \frac{\partial^2\tilde{v}}{\partial y\partial x} & \frac{\partial^2\tilde{v}}{\partial y^2} & \frac{\partial^2\tilde{v}}{\partial y\partial z} \\ \frac{\partial^2\tilde{v}}{\partial z\partial x} & \frac{\partial^2\tilde{v}}{\partial z\partial y} & \frac{\partial^2\tilde{v}}{\partial z^2} \end{bmatrix},$$

$$\mathbf{H}_{\tilde{w}} = \begin{bmatrix} \frac{\partial^2\tilde{w}}{\partial x^2} & \frac{\partial^2\tilde{w}}{\partial x\partial y} & \frac{\partial^2\tilde{w}}{\partial x\partial z} \\ \frac{\partial^2\tilde{w}}{\partial y\partial x} & \frac{\partial^2\tilde{w}}{\partial y^2} & \frac{\partial^2\tilde{w}}{\partial y\partial z} \\ \frac{\partial^2\tilde{w}}{\partial z\partial x} & \frac{\partial^2\tilde{w}}{\partial z\partial y} & \frac{\partial^2\tilde{w}}{\partial z^2} \end{bmatrix},$$

and $\mathbf{J}_{\tilde{\mathbf{u}}}$, $\mathbf{J}_{\tilde{\mathbf{v}}}$, and $\mathbf{J}_{\tilde{\mathbf{w}}}$ as defined in Eq. (A2).

Given the Cartesian pressure gradient $\nabla p = \left(\frac{\partial p}{\partial x}, \frac{\partial p}{\partial y}, \frac{\partial p}{\partial z}\right)$ and using the chain rule, the components of the pressure gradient in local coordinates can be calculated as

$$\frac{\partial p}{\partial s} = \nabla p\cdot\frac{\partial\mathbf{x}}{\partial s},\qquad \frac{\partial p}{\partial r} = \nabla p\cdot\frac{\partial\mathbf{x}}{\partial r},\qquad \frac{\partial p}{\partial\theta} = \nabla p\cdot\frac{\partial\mathbf{x}}{\partial\theta},$$

with $\frac{\partial\mathbf{x}}{\partial s}$, $\frac{\partial\mathbf{x}}{\partial r}$, and $\frac{\partial\mathbf{x}}{\partial\theta}$ given by Eqs. (A2).

[1] K. Perktold, M. Resch, and R. Peter, "3-D numerical analysis of pulsatile flow and wall shear stress in the carotid artery bifurcation," J. Biomech. **24**, 409–420 (1991).
[2] Y. Papaharilaou, D. J. Doorly, and S. J. Sherwin, "The influence of out-of-plane geometry on pulsatile flow within a distal end-to-side anastomosis," J. Biomech. **35**, 1225–1239 (2002).
[3] D. A. Steinman, "Image-based computational fluid dynamics modeling in realistic arterial geometries," Ann. Biomed. Eng. **30**, 483–497 (2002).
[4] L. Grinberg, T. Anor, J. Madsen, A. Yakhot, and G. E. Karniadakis, "Large-scale simulation of the human arterial tree," Clin. Exp. Pharmacol. Physiol. **36**, 194–205 (2009).
[5] C. G. Caro, J. M. Fitzgerald, and R. C. Schroter, "Atheroma and arterial wall shear. Observation, correlation and proposal of a shear dependent mass transfer mechanism for atherogenesis," Proc. R. Soc., London, Ser. B **177**, 109–133 (1971).
[6] A. M. Malek, S. L. Alper, and S. Izumo, "Hemodynamic shear stress and its role in atherosclerosis," JAMA, J. Am. Med. Assoc. **282**, 2035–2042 (1999).
[7] C. G. Caro, N. J. Cheshire, and N. Watkins, "Preliminary comparative study of small amplitude helical and conventional ePTFE arteriovenous shunts in pigs," J. R. Soc. Interface **2**, 261–266 (2005).
[8] J. Eustice, "Experiments on stream-line motion in curved pipes," Proc. R. Soc. London, Ser. A **85**, 119–131 (1911).
[9] J. Eustice, "Flow of water in curved pipes," Proc. R. Soc. London, Ser. A **84**, 107–118 (1910).
[10] W. R. Dean, "Note on the motion of fluid in a curved pipe," Philos. Magn. Ser. 7 **4**, 208–223 (1927).
[11] W. R. Dean, "The stream-line motion of fluid in a curved pipe," Philos. Magn. Ser. 7 **5**, 673–695 (1928).
[12] F. T. Smith, "Fluid flow into a curved pipe," Proc. R. Soc. London, Ser. A **331**, 71–87 (1976).
[13] Y. Agrawal, L. Talbot, and K. Gong, "Laser anemometer study of flow development in curved pipes," J. Fluid Mech. **85**, 497–518 (1978).
[14] T. J. Pedley, "*The fluid mechanics of large blood vessels*," (Cambridge University Press, Cambridge, 1980), p. 446.
[15] S. A. Berger, L. Talbot, and L.-S. Yao, "Flow in curved pipes," Annu. Rev. Fluid Mech. **15**, 461–512 (1983).
[16] P. H. M. Bovendeerd, A. A. van Steenhoven, F. N. van de Vosse, and G. Vossers, "Steady entry flow in a curved pipe," J. Fluid Mech. **177**, 233–246 (1987).
[17] J. H. Siggers and S. L. Waters, "Steady flows in pipes with finite curvature," Phys. Fluids **17**, 077102 (2005).
[18] R. Pitt, "Numerical simulation of fluid mechanical phenomena in idealised physiological geometries: stenosis and double bend," Ph.D. thesis (Imperial College London, University of London, 2005).
[19] O. Boiron, V. Deplano, and R. Pelissier, "Experimental and numerical studies on the starting effect on the secondary flow in a bend," J. Fluid Mech. **574**, 109–129 (2007).
[20] M. Germano, "On the effect of torsion on a helical pipe flow," J. Fluid Mech. **125**, 1–8 (1982).
[21] L. Zabielski and A. J. Mestel, "Steady flow in a helically symmetric pipe," J. Fluid Mech. **370**, 297–320 (1998).
[22] L. Zabielski and A. J. Mestel, "Unsteady blood flow in a helically symmetric pipe," J. Fluid Mech. **370**, 321–345 (1998).
[23] A. N. Cookson, D. J. Doorly, and S. J. Sherwin, "Mixing through stirring of steady flow in small amplitude helical pipes," Ann. Biomed. Eng. **37**, 710–721 (2009).
[24] K. R. Moyle, L. Antiga, and D. A. Steinman, "Inlet conditions for image-based CFD models: is it reasonable to assume fully-developed flow? J. Biomech. Eng. **128**, 371–379 (2006).
[25] K. E. Lee, K. H. Parker, C. G. Caro, and S. J. Sherwin, "The spectral/*hp* element modelling of steady flow in non-planar double bends," Int. J. Numer. Methods Fluids **57**, 519–529 (2008).
[26] P. E. Vincent, A. M. Plata, A. A. E Hunt, P. D. Weinberg, and S. J. Sherwin, "Blood flow in the rabbit aortic arch and descending thoracic aorta," J. R. Soc., Interface **8**, 1708–1719 (2011).
[27] U. Morbiducci, D. Gallo, R. Ponzini, D. Massai, L. Antiga, F. M. Montevecchi, and A. Redaelli, "Quantitative analysis of bulk flow in image-based hemodynamic models of the carotid bifurcation: The influence of outflow conditions as test case," Ann. Biomed. Eng. **38**, 3688–3705 (2010).
[28] U. Morbiducci, R. Ponzini, G. Rizzo, M. Cadioli, A. Esposito, F. M. Montevecchi, and A. Redaelli, "Mechanistic insight into the physiological relevance of helical blood flow in the human aorta: an in vivo study," Biomech. Model Mechanobiol. **10**, 339–355 (2011).
[29] X. Liu, Y. Fan, X. Deng, and F. Zhan, "Effect of non-Newtonian and pulsatile blood flow on mass transport in the human aorta," J. Biomech. **44**, 1123–1131 (2011).
[30] U. Morbiducci, D. Gallo, D. Massai, R. Ponzini, M. Deriu, L. Antiga, A. Redaelli, and F. M. Montevecchi, "On the importance of blood rheology for bulk flow in hemodynamic models of the carotid bifurcation," J. Biomech. **44**, 2427–2438 (2011).
[31] J. Jeong and F. Hussain, "On the identification of a vortex," J. Fluid Mech. **285**, 69–94 (1995).
[32] S. C. Shadden and C. A. Taylor, "Characterization of coherent structures in the cardiovascular system," Ann. Biomed. Eng. **36**, 1152–1162 (2008).
[33] S. C. Shadden, M. Astorino, and J. F. Gerbeau, "Computational analysis of an aortic valve jet with Lagrangian coherent structures," Chaos **20**, 017512 (2010).
[34] G. E. Karniadakis and S. J. Sherwin, *Spectral/hp Element Methods for Computational Fluid Dynamics* (Oxford University Press, New York, 2005).
[35] D. A. McDonalds, *Blood Flow in Arteries* (Edward Arnold, London, 1974).
[36] G. K. Batchelor, *An Introduction to Fluid Mechanics, App. 2* (Cambridge University Press, Cambridge, 1967).
[37] D. J. Doorly and S. J. Sherwin, "Geometry and flow," *Cardiovascular Mathematics. Modeling and Simulation of the Circulatory System*, edited by L. Formaggia, A. Quarteroni, and A. Veneziani (Springer-Verlag, Milan, 2009), pp. 177–209.
[38] D. J. Doorly, S. J. Sherwin, P. T. Franke, and J. Peiró, "Vortical flow structure identification and flow transport in arteries," Comput. Methods Biomech. Biomed. Eng. **5**, 261–275 (2002).

[39] L.-S. Yao and S. A. Berger, "Entry flow in a curved pipe," J. Fluid Mech. **67**, 177–196 (1975).
[40] U. S. Choi, L. Talbot, and I. Cornet, "Experimental study of wall shear rates in the entry region of a curved tube," J. Fluid Mech. **93**, 465–489 (1979).
[41] L. Talbot and S. J. Wong, "A note on boundary layer collision in a curved pipe," J. Fluid Mech. **122**, 505–510 (1982).
[42] G. Rappitsch and K. Perktold, "Computer simulation of convective diffusion processes in large arteries," J. Biomech. **29**, 207–216 (1995).
[43] D. A. Steinman and C. R. Ethier, "The effect of wall distensibility on flow in a two-dimensional end-to-end anastomosis," J. Biomech. Eng. **116**, 294–301 (1994).
[44] J. Alastruey, K. H. Parker, J. Peiró, and S. J. Sherwin, "Analysing the pattern of pulse waves in arterial networks: a time-domain study," J. Eng. Math. **64**, 331–351 (2009).
[45] J. Alastruey, A. W. Khir, K. S. Matthys, P. Segers, S. J. Sherwin, P. Verdonck, K. H. Parker, and J. Peiró, "Pulse wave propagation in a model human arterial network: Assessment of 1-D visco-elastic simulations against *in vitro* measurements," J. Biomech. **44**, 2250–2258 (2011).
[46] See supplementary material at http://dx.doi.org/10.1063/1.3694526 for abbreviations used in the paper.